Reducing Mechanical and Flow-Induced Noise in the Surface Suspended Acoustic Receiver

by

Jason I. Gobat

B.S., University of California, San Diego (1993)
B.A., University of California, San Diego (1993)

Submitted to the
Department of Applied Ocean Physics and Engineering, WHOI
and the
Department of Ocean Engineering, MIT
in partial fulfillment of the requirements for the degree of

Master of Science in Oceanographic Engineering

at the

MASSACHUSETTS INSTITUTE OF TECHNOLOGY
and the
WOODS HOLE OCEANOGRAPHIC INSTITUTION

May 1997

© Massachusetts Institute of Technology 1997. All rights reserved.

Author ....
Department of Applied Ocean Physics and Engineering, WHOI
Department of Ocean Engineering, MIT
May 6, 1997

Certified by . .....
Dr. Mark A. Grosenbaugh
Associate Scientist
Thesis Supervisor

MASSACHUSETTS INSTITUTE OF TECHNOLOGY

JUL 15 1997

LIBRARIES

Accepted by ....
Prof. Henrik Schmidt
Chairman, Joint Committee on Oceanographic Engineering

Eng.

Reducing Mechanical and Flow-Induced Noise in the Surface Suspended Acoustic Receiver

by

Jason I. Gobat

Submitted to the
Department of Applied Ocean Physics and Engineering, WHOI
and the
Department of Ocean Engineering, MIT
on May 6, 1997, in partial fulfillment of the
requirements for the degree of
Master of Science in Oceanographic Engineering

Abstract

The Surface Suspended Acoustic Receiver (SSAR) is a free-drifting platform intended for use as a receiver in large scale acoustic tomography experiments. Early prototypes of the SSAR exhibited very poor signal-to-noise ratios in the frequency band of the hydrophones. This thesis details efforts to reduce the hydrophone noise level by combining the analysis of experimental data with the results from numerical models.

Experiments were conducted to quantify both the frequency content and magnitude of noise generated on the SSAR. Through a program of sea trials and pond testing, two noise sources were identified. The dominant source of noise in the SSAR is velocity dependent flow noise that results from turbulent pressure fluctuations on the hydrophones. A second noise source results from the acceleration sensitivity of the hydrophones in conjunction with high frequency accelerations present in the hydrophone array cable. These high frequency accelerations also show a velocity dependence. The presence of the acceleration-induced noise leads to correlations between the signals from adjacent hydrophones, thus distorting the typical picture that flow noise should be uncorrelated along an array. The primary methods of eliminating the noise are encapsulating the hydrophone in a flow shield, eliminating the array cable, and slowing the system down by replacing the wave following surface buoy with a spar buoy.

Using the experimental results, empirical relationships between hydrophone velocity and expected noise level are formed for both shielded and unshielded hydrophones. The numerical models developed as a part of this effort are then used to predict the velocities for a wide range of possible SSAR configurations. The models can also provide information, such as system tensions, that is useful in evaluating the longevity and survivability of SSARs. Modeled design fixes include subsurface component changes as well as comparing a wave following surface buoy to a spar buoy.

Thesis Supervisor: Dr. Mark A. Grosenbaugh
Title: Associate Scientist

Acknowledgments

This thesis has been in the works for some time now – largely because it is difficult to write a story that simply refuses to come to a satisfactory end. I have been involved with the SSAR project for two years and I have to express my gratitude to the others on the team who have given me an appreciation of the difficulties associated with the development of functional, survivable oceanographic systems. The opportunity for experience and interaction in technical areas and with people that I would not normally have contact with in my role as a student has been enormously satisfying for me. It is opportunities like this that I believe are the greatest strength of the Joint Program and why I came to Woods Hole in the first place.

My advisor, Mark Grosenbaugh, first presented the problem to me and has been a thoughtful and constructive contributor to the solutions presented herein. Lee Freitag of the Advanced Engineering Laboratory has been very generous in his patient explanations of the acoustics and instrumentation behind the SSAR. I am particularly grateful to Lee for the opportunities to be a part of the experimental efforts - both on land and at sea. Most of what little I have learned about the mechanical details of buoy systems I owe to Walter Paul of the Buoy and Mooring Systems Laboratory and Richard Arthur of the Advanced Engineering Laboratory. Bill Webster from the University of California, Berkeley was the person who got us away from chasing high frequency accelerations and got us into doing something about low frequency velocity – a step that has proved crucial in getting us on the path to actually getting this thing working. Dan Merdes from the Applied Research Laboratory at Pennsylvania State University coordinated much of the experimental work at Aberdeen Test Center.

My opportunity to work on the SSAR is due in large part to the flexibility provided by the funding support that I have received through the Office of Naval Research Graduate Fellowship Program. The SSAR project at WHOI is sponsored by the Advanced Research Projects Agency under grant MDA 972-93-1-0004.

Finally of course, the obligatory (and yet truly heartfelt) thanks to my wife, Allison. Without her support this whole graduate school thing would feel a whole lot more like graduate school and a whole lot less like the great adventure that it has become.

Contents

List of Figures

List of Tables

Chapter 1

Introduction

Acoustic tomography is a process whereby measurements of sound speed are used to determine thermal properties of the ocean. In the ATOC (Acoustic Thermometry of Ocean Climate) and GAMOT (Global Acoustic Mapping of Ocean Temperature) projects sound sources off the California and Hawaii coasts broadcast acoustic signals to receivers which are located throughout the Pacific ocean, some of them thousands of kilometers away. In the case of the ATOC project, these receivers are fixed subsurface moorings (VLAs – Vertical Line Arrays) and U.S. Navy hydrophone listening stations [4, 11]; in the case of the VLAs the data is collected only sporadically through the use of pop-up buoys.

The receiver concept chosen for the GAMOT project uses an entirely different approach. The receivers in this case are relatively inexpensive surface-coupled drifting systems. The possible advantages with this approach are enlarged spatial coverage due in part to the movement of the arrays around the ocean and in part to the increased number of receivers that can be deployed as a result of their low cost. The surface-coupling, necessitated by accurate position fixes via GPS, also allows for near real-time telemetry of data via ARGOS transmission [6, 17].

The problem with the SSAR that this thesis seeks to address is an artifact of this surface coupling. As the SSAR moves up and down at wave frequencies, the array (and the attached hydrophones) move with vertical velocities that can approach 2 m/s in relatively light seas. During the initial design phase, these motions were considered unimportant because the wave frequencies are well below the acoustic band of the hydrophones. However, this

analysis overlooked noise mechanisms which can transfer the low frequency wave motions into higher frequency mechanical and acoustic signals. These higher frequency noise signals, which have as their ultimate source the low frequency, wave-induced motions of the SSAR, are present throughout the acoustic band of the hydrophone.

1.1 Current SSAR design

The original SSAR design is shown in figure 1-1. This design will serve as the baseline against which design changes are made and performance improvements are measured. The system consists of a cylindrical surlyn foam surface buoy, approximately 1.2 m in diameter and 0.75 m in height. The snubber hose is a hollow rubber hose, laid-up out of tire cord and steel reinforcement. The conductors run through the hose via a tightly wound, spring-like, coil-cord arrangement. The idea behind the snubber is to provide a rugged, compliant conductor between the surface buoy and the subsurface components. It was originally hoped that the hose would provide enough compliance so as to decouple the motions of the subsurface components from the motions of the surface buoy. The subsurface float is a fiberglass-wrapped surlyn sphere, 0.7 m in diameter. The primary depth and strength member for the SSAR is the 500 m long plastic coated, double-armored, three conductor electromechanical (EM) cable. Subsurface electronics are housed in a 1.8 m long, 0.25 m diameter stainless steel pressure case. The top of this case also holds the ultra-short baseline array which is used to acoustically locate the array relative to the surface buoy for accurate position fixing of the array. The acoustic array consists of a core of conductors wrapped by a kevlar strength member, a nylon overbraid and a fuzzy fairing. At the bottom of the array is 10 m of wire rope running down to the depressor weight [7, 6].

1.2 Hydrophone noise

The need for modifications to the baseline SSAR configuration pictured in figure 1-1 became apparent after analysis of the hydrophone time series from at sea testing of prototype models. Figure 1-2 shows the time series from one hydrophone over a two minute period with no source signal present. The impulsive spikes represent serious noise contamination.

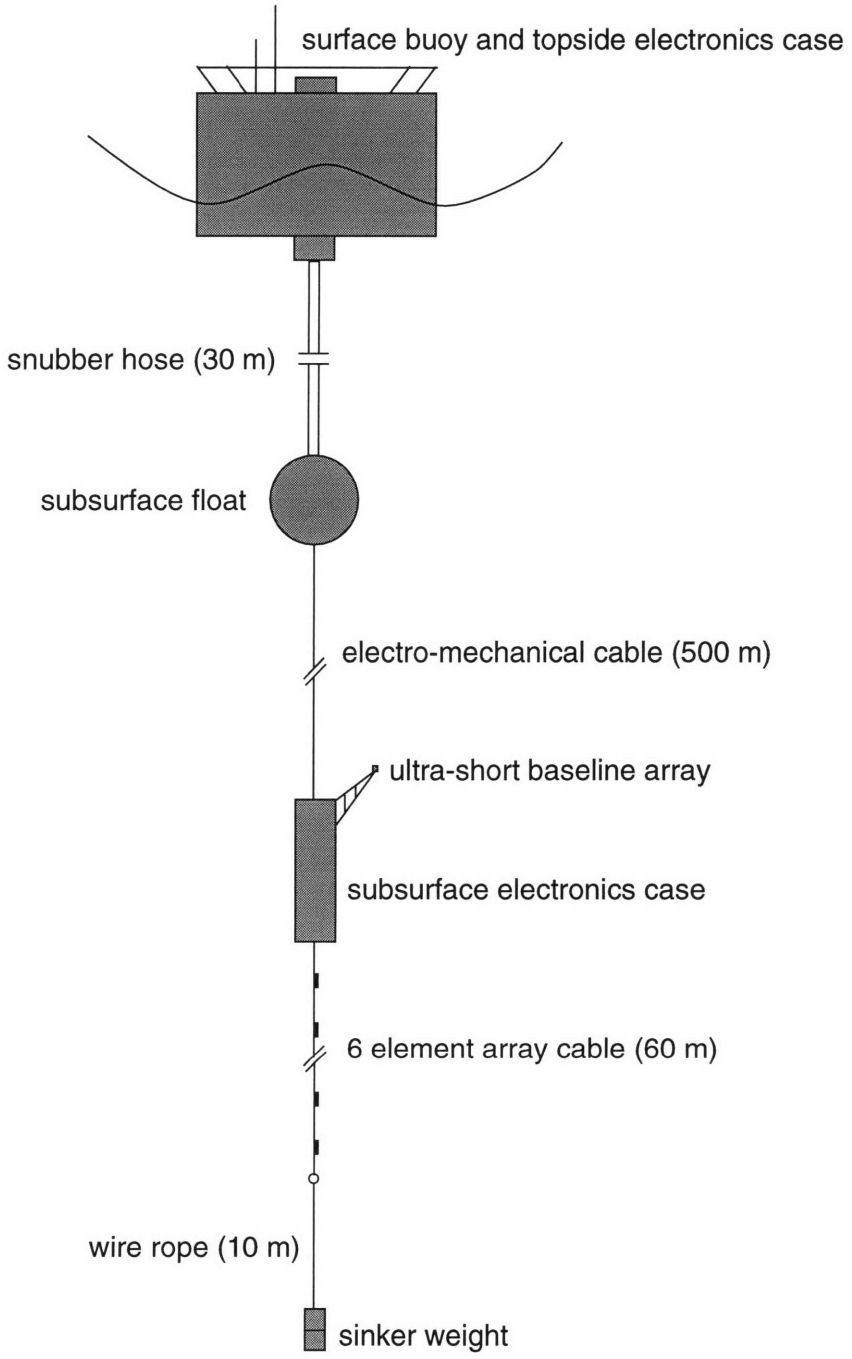

Figure 1-1: The current standard SSAR design.

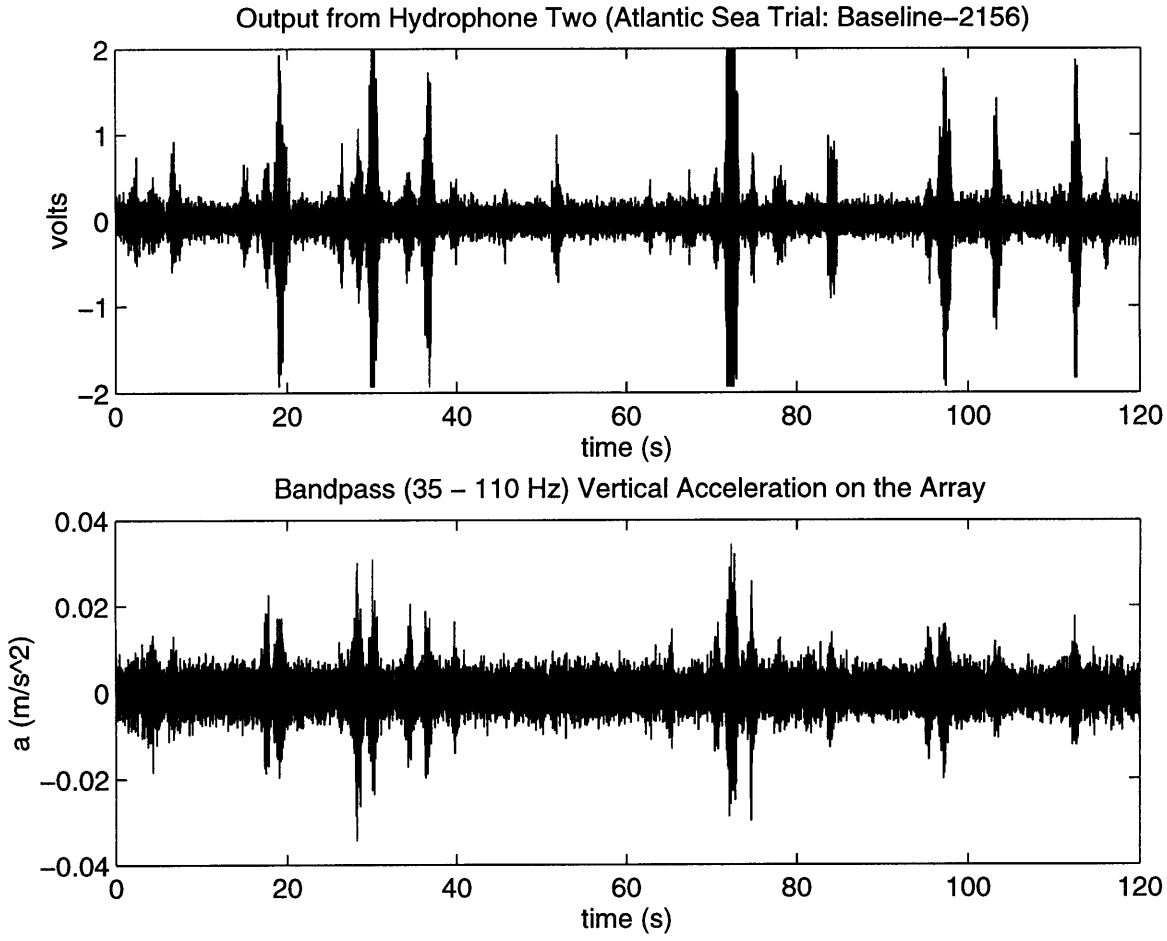

Figure 1-2: Hydrophone and bandpass accelerometer time series from at-sea testing of the baseline SSAR configuration.

In terms of acoustic level, they represent a hydrophone response of 100 – 120 dB re μPa; signal levels from the source at ranges of 2000 – 3000 km, after array and averaging gains are applied, will be at best between 80 and 90 dB re μPa, undetectable given the noise levels in the baseline design.

The bottom plot of figure 1-2 shows the bandpass filtered acceleration time series from an accelerometer placed near the first hydrophone on the array cable. The bandpass filtered data reflects the acceleration energy in the same frequency band as the acoustic response of the hydrophones. There is clearly a coincidence between impulsive high frequency acceleration events and the impulsive spikes in the hydrophone time series. This suggests that the

hydrophone noise may be, at least in part, due to hydrophone sensitivity to accelerations and the presence of a mechanism for the generation of high frequency accelerations.

1.3 History of noise mitigation efforts

1.3.1 Snap loads

One such possible mechanism for the generation of high frequency accelerations given forcing only at much lower ocean wave frequencies is snap loading. Snap loads occur when the low frequency (wave-induced) motions of the system are such that one or more of the cable segments in the system goes slack and then retensions. At the moment of retensioning, an impulsive load, with broadband frequency content, is generated.

Early model results indicated that even in relatively light seas system motions were large enough to create slack events in the snubber hose and that these snaps were capable of generating high frequency accelerations at the hydrophones. In light of this result, increasing the sinker weight to add additional static tension throughout the system was proposed as a simple and cost-effective way to reduce the noise. This hypothesis was tested during sea trials by deploying both a baseline SSAR and a SSAR with an extra 400 pounds at the sinker.

The baseline results from these tests are shown in figure 1-3. The top plot shows the accelerations measured at the subsurface float (the bottom of the snubber hose); the second plot shows the same accelerations bandpass filtered into the 35 – 110 Hz band of the hydrophones. The very large spikes are evidence of the float being jerked around by impulsive snap loading. Many of the snaps at the subsurface float also appear to correspond to noise spikes in the hydrophone data.

The results from the tests with additional sinker weights are shown in figure 1-4. In this case, the snap loads appear to have been eliminated, just as the model predicted. However, the hydrophone noise actually seems to have gotten worse – with some noise spikes so large that they are clipped (at ± 2 volts).

In reviewing the model results in light of the at-sea test data, it is obvious that by underestimating the damping in the EM cable the effects of snap loading were overestimated.

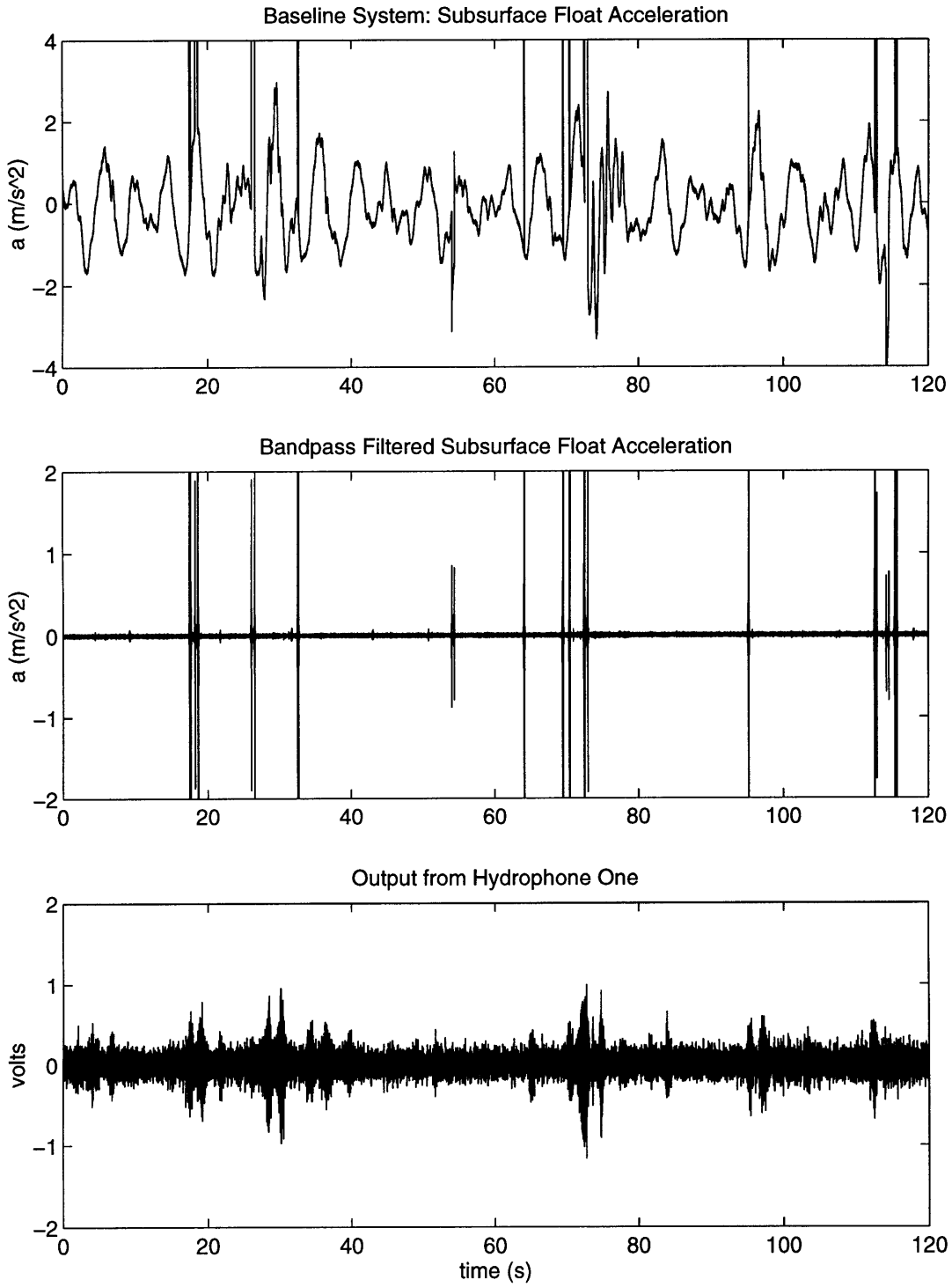

Figure 1-3: Illustration of snap loads during at-sea testing of the baseline SSAR configuration.

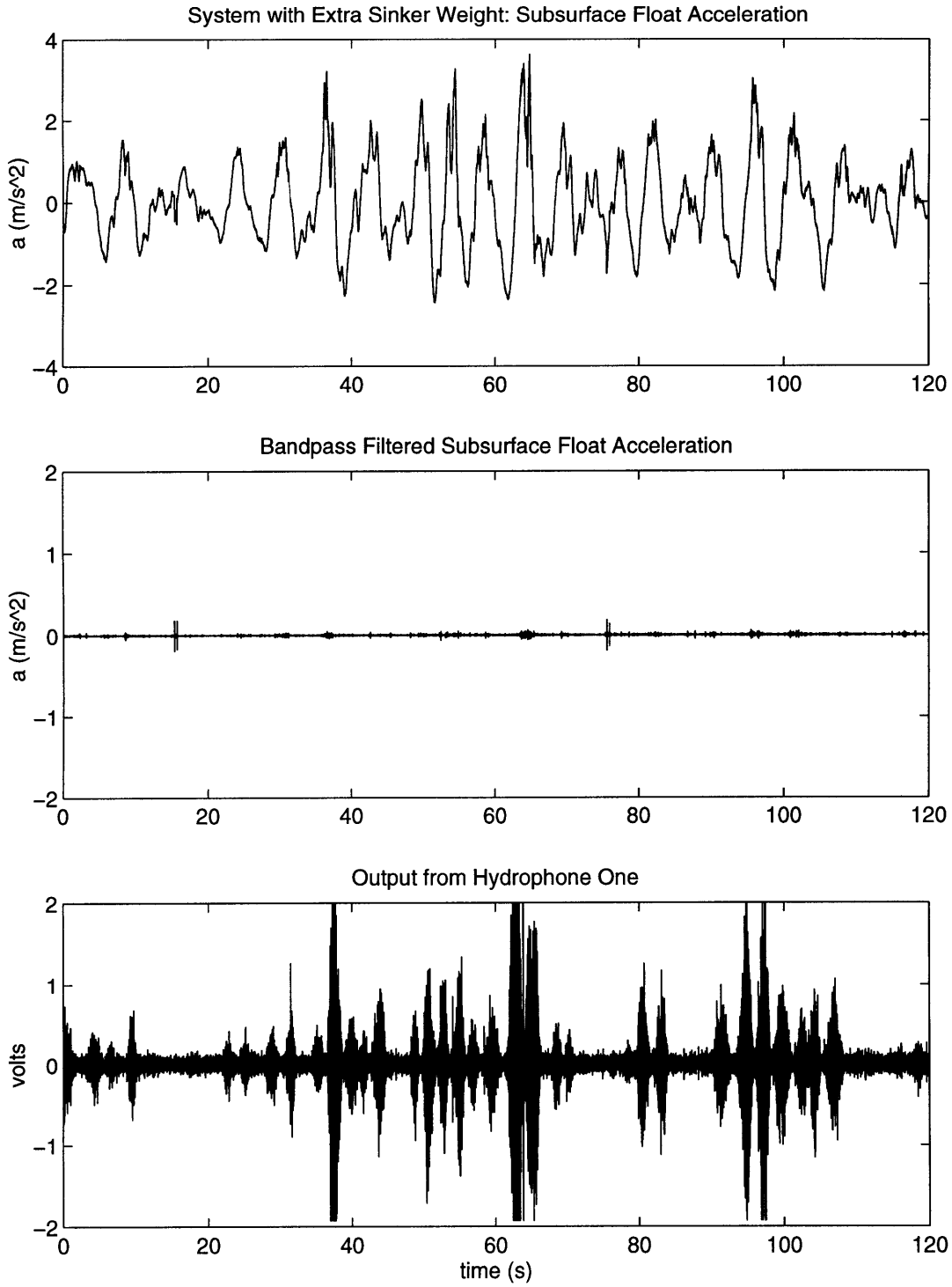

Figure 1-4: Acceleration and hydrophone time series from the system deployed with extra sinker weight to reduce snap loading.

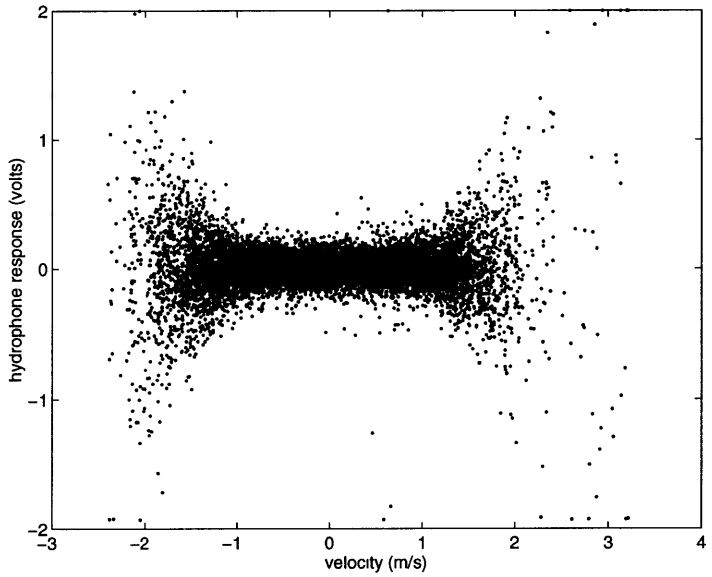

Figure 1-5: Scatter plot showing the relationship between array vertical velocity and hydrophone noise level.

The snap loading hypothesis was only partially correct. There were snap loads in the system, but they were not a significant cause of the high frequency accelerations at the hydrophones. It is important to note, however, that eliminating the snaps is still a desirable goal because the large tension spikes associated with a snap load can lead to ultimate or fatigue failure of system components.

1.3.2 Recent efforts

Subsequent analysis of the data from the sea trials showed that in addition to being coincident with impulsive high frequency accelerations, the hydrophone noise was strongly linked to the low frequency, wave-induced vertical velocities of the hydrophones. An illustration of this link is shown in figure 1-5 which shows the hydrophone signal level plotted against array vertical velocity for a random sampling of data points from four different time series, covering two distinct SSAR configurations. Such a relationship between acoustic noise level and the velocity of the hydrophone elements through the water is suggestive of flow-induced noise.

	hydrophone 1	hydrophone 2	hydrophone 3
hydrophone 2	0.612	x	x
hydrophone 3	0.402	0.605	x
hydrophone 4	0.176	0.324	0.698

Table 1.1: Cross-correlations between hydrophone time series from a 20 second time period with minimal clipping in all four hydrophone channels. The data is taken from a baseline deployment during the September, 1995 sea trials.

Flow noise results from the irregular flow over the hydrophones and the subsequent formation of turbulent eddies. The near-field, pseudo-sound portion of the flow noise results from the pressure fluctuations exciting vibrations in the hydrophone wall; these pressure induced vibrations result in a signal from the hydrophone element (which is after all nothing more than a pressure level sensor). There is also a radiated, far-field (true sound) component of flow noise which results from the coupling of the turbulent fluctuations into propagating acoustic modes. This second type of flow noise is relatively weak in comparison to the noise generated in the near-field, especially at low velocities and low frequencies [9, 12].

That the dominant source of noise may be flow noise is one of the critical lessons that can be learned from the SSAR noise reduction effort. Flow noise was initially ruled out as a noise source because the noise between hydrophones was correlated. Given a portion of data with relatively little clipping in the hydrophone signals, the cross-correlations between adjacent hydrophones are quite high (table 1.1). For the full time series (i.e., keeping portions that have clipped data in them) the correlations are still as high as 0.2 and 0.3. Because flow noise results from a localized, turbulent process, it will generally appear as uncorrelated along the length of an array. That the hydrophone signals are sometimes well correlated on the SSAR suggests that the acceleration-induced component of noise imposes a degree of correlation on the total noise signal.

A second reason that flow noise was at first discounted as a possible noise source was the early failure of attempts to shield the hydrophones from flow noise. Immediately after the link between noise and low frequency velocity became apparent, a design modification was made which encapsulated each hydrophone in a two inch diameter rigid tube with faired endcaps. Encapsulating the entire array in a smooth urethane tube was also tried.

Both of these designs were sea tested, neither resulting in any noise reduction[1]. The early attempts at shielding were made before there was an accurate picture of just what the noise sources were; when the shielding did not eliminate the noise, the early conclusion was that there must not have been any flow noise to eliminate, rather than the conclusion that the flow shielding simply was not adequate. Better experimental evidence is now available which indicates that the primary source of noise on the SSAR is flow noise; evidence is also available to indicate the level of flow shielding that is necessary to reduce the flow noise on the SSAR.

1.4 Design variations

Howe *et al* [10] proposed a spar buoy for their acoustic tomography drifter in order to minimize hydrophone motions. For this same reason, one of the major design changes considered for the SSAR is replacing the current surface buoy with a spar buoy. As an alternative, less radical, velocity reduction measure, the effect of a second snubber hose in series with the first is explored.

In addition to lowering velocities, there is both theoretical and experimental evidence that the near-field component of flow noise can be reduced asymptotically to zero by increasing the hydrophone size [9]. To apply this idea to the SSAR, the six element array can be replaced by a single, flow-shielded hydrophone rigidly mounted to the bottom of the subsurface pressure case. The flow shield will effectively increase hydrophone size by increasing the separation between the flow and the hydrophone element. This approach to the flow shield avoids the problems of the early flow shield designs because the flow shield can be made much larger (thus removing the hydrophone much further away from the flow) once the hydrophone is removed from the array.

Design modifications to reduce snap loading include increasing sinker weight and removing the subsurface float. All of these changes have advantages and disadvantages in terms of cost, ease of implementation, longevity of the systems when deployed, and ultimately, effectiveness as a noise reduction measure.

[1] In fact, the noise appeared to get worse, perhaps due to increased acceleration-induced noise.

1.5 Overview of the thesis

Chapter 2 gives the details for the time- and frequency-domain numerical models that were developed to simulate the vertical motions, accelerations, velocities and tensions of the SSAR over a wide range of configurations. Chapter 3 presents the methods and results from the experiments which were used to identify and quantify the sources of the high frequency noise in the hydrophones. In chapter 4, the experimental results are combined with results from the numerical model to develop a noise model that can be used to quantify the expected noise level in a variety of proposed SSAR configurations. Conclusions and recommendations for future work are presented in chapter 5.

Chapter 2

Numerical models

Both frequency- and time-domain models were used to analyze the SSAR. Frequency domain models are useful for design studies in that they can give a quick, statistical picture of basic system behavior. Given a high sea state ocean storm as input, the frequency domain model can be used to compute a spectrum of tension. From this spectrum, a statistical maximum design tension is easily calculated. The frequency domain tension results can also be used to derive a statistical measure of the probability of snap loading. Given a sea spectrum that describes typical operating conditions, the frequency domain model can predict the root mean square velocities of the system components or the frequency with which certain critical velocity transition points are exceeded under those conditions.

The time domain model is useful for analyzing nonlinear behaviors that cannot be fully analyzed with the frequency domain model, such as snap loads. The time domain model results also provide the input into empirically determined predictors of noise level on the SSAR. These relationships are derived from experimentally collected time series and are thus most easily applied to time domain data.

2.1 Frequency domain model

The idealization and numbering scheme for both frequency and time domain models is shown in figure 2-1. The frequency domain model considers the system as a series of n continuous elastic segments (snubber hose, EM cable, array, and wire rope) with lumped

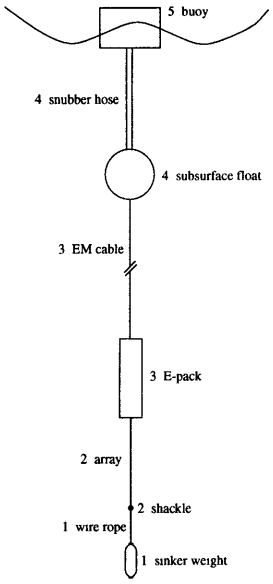

Figure 2-1: Idealized model and numbering scheme for the SSAR system. Note that the numbering for both masses and cable segments proceeds from the sinker upwards, not from the surface downwards.

masses (subsurface float, E-pack, shackle, and sinker weight) at the bottom of the various segments and a surface buoy at the top of segment n. For each segment j and each mass at the bottom of that segment the following definitions are made. $u_j(z_j, t)$ is the displacement coordinate from the equilibrium position along the segment (z_j is positive up and has its origin at the bottom end of the segment). $U_j(t)$ is the displacement of the mass from equilibrium. m_j, b_j, and r_j are the mass, equivalent linearized damping constant, and structural damping constant (all per unit length) of the segment. M_j and B_j are the virtual mass and equivalent linear damping constant of the lumped mass; EA_j is the axial stiffness of the segment. L_j is the length of the segment.

At the sinker weight (the terminal lumped mass), the equation of dynamic equilibrium is

$$M_1 \frac{d^2 U_1}{dt^2} + B_1 \frac{dU_1}{dt} = EA_1 \left. \frac{\partial u_1}{\partial z_1} \right|_{z_1=0} . \tag{2.1}$$

For any other submerged lumped mass (the E-pack or the subsurface float),

$$M_j \frac{d^2U_j}{dt^2} + B_j \frac{dU_j}{dt} = EA_j \left.\frac{\partial u_j}{\partial z_j}\right|_{z_j=0} - EA_{j-1} \left.\frac{\partial u_{j-1}}{\partial z_{j-1}}\right|_{z_{j-1}=L_{j-1}}, \tag{2.2}$$

and for the surface buoy the expression of equilibrium is

$$M_B \frac{d^2U_B}{dt^2} + B_B \frac{dU_B}{dt} + \rho g A_{\text{wp}} U_B = -EA_n \left.\frac{\partial u_n}{\partial z_n}\right|_{z_n=L_n} + F_B(t), \tag{2.3}$$

where $F_B(t)$ is the wave force on the surface buoy and A_{wp} is the waterplane area of the surface buoy. Along any segment j the equilibrium condition is stated as

$$m_j \frac{\partial^2 u_j}{\partial t^2} + (b_j + r_j) \frac{\partial u_j}{\partial t} = EA_j \frac{\partial^2 u_j}{\partial z_j^2}. \tag{2.4}$$

Assuming harmonic forcing at the buoy with magnitude $\hat{F}_B$ and corresponding harmonic solutions for the displacements throughout the system, the solutions will be of the form

$$u_j(z_j, t) = e^{i\omega t} \left[C_{2j-1} \cos k_j z_j + C_{2j} \sin k_j z_j\right], \tag{2.5}$$

and

$$U_j(t) = \hat{U}_j e^{i\omega t}, \tag{2.6}$$

where the C_j and $\hat{U}_j$ are complex constants to be determined and

$$k_j = \sqrt{\frac{m_j\omega^2 - i\omega\,(b_j + r_j)}{EA_j}}. \tag{2.7}$$

After substituting equations 2.5 and 2.6 into the equilibrium equations (equations 2.1 through 2.4) the time dependence can be eliminated by dividing through by the exponential term. By then taking advantage of the fact that $u_j(0) = U_j$ (and thus the fact that $\hat{U}_j = C_{2j-1}$) the following linear system of equations can be derived

$$
\begin{aligned}
0 &= C_1\left(-\omega^2 M_1 + i\omega B_1\right) - C_2 EAk_1, \qquad (2.8)\\
0 &= C_1 \cos kL_1 + C_2 \sin kL_1 - C_3,\\
0 &= -C_1 EAk_1 \sin kL_1 + C_2 EAk_1 \cos kL_1 + C_3\left(-\omega^2 M_2 + i\omega B_2\right) - C_4 EAk_2,\\
0 &= C_3 \cos kL_2 + C_4 \sin kL_2 - C_5,\\
\vdots &= \vdots\\
0 &= -C_{2n-3} EAk_{n-1} \sin kL_{n-1} + C_{2n-2} EAk_{n-1} \cos kL_{n-1}\\
&\quad + C_{2n-1}\left(-\omega^2 M_n + i\omega B_n\right) - C_{2n} EAk_n,\\
0 &= C_{2n-1} \cos kL_n + C_{2n} \sin kL_n - \hat{U}_B,\\
\hat{F}_B &= -C_{2n-1} EAk_n \sin kL_n + C_{2n} EAk_n \cos kL_n + \hat{U}_B\left(-\omega^2 M_n + i\omega B_n + \rho g A_{\mathrm{wp}}\right).
\end{aligned}
$$

As a system in $2n+1$ equations and $2n+1$ unknowns, the magnitude of the response at any of the lumped masses at a given excitation frequency, ω, can be determined by solving this linear system for C_1 through C_{2n} and $\hat{U}_B$. Transfer functions can be constructed for the various system components to harmonic wave forcing by solving the system over a range of frequencies assuming a unit force magnitude at each frequency.

2.1.1 Linearized damping

Because the desired result from the model is the response of the SSAR system to a random sea, the output of the model needs to be a transfer function that can be used in linear system theory along with an input spectrum to calculate the performance measures that will quantify the merits of a given design. For this purpose, the damping coefficients must be linearized in a way that accounts for the nonharmonic nature of the input spectra. In such a case, the damping constants are linearized in terms of spectral parameters and are given by Faltinsen [3]

$$
b_{\mathrm{eq}} = 2\sigma_v \sqrt{\frac{2}{\pi}} \left(\frac{1}{2}\rho C_f \pi d\right), \qquad (2.9)
$$

$$
B_{\mathrm{eq}} = 2\sigma_v \sqrt{\frac{2}{\pi}} \left(\frac{1}{2}\rho C_D S\right), \qquad (2.10)
$$

where C_D is the bluff body drag coefficient for a massive system component, S is the projected frontal surface area of the component, C_f is the frictional drag coefficient of a cable segment, d is

the diameter of that segment and σ_v is the standard deviation of the velocity for that component.

With this linearization, the solution process must be iterative. An output spectrum is assumed and an initial value for σ_v calculated. The resulting linearized damping coefficients are used in the calculation of the motion at a series of frequencies. The resulting transfer function and the input spectrum are then used to calculate the actual output spectrum and corresponding value of σ_v. The iteration stops when the calculated and guessed values of σ_v converge.

2.2 Time domain model

The time domain model is also based on the idea of a series of continuous elastic members with additional lumped mass (and drag) at the connection between segments. In the time domain, however, each elastic member is treated as a sequence of idealized one-dimensional mass-less springs with small lumped masses at the nodes between springs. The system is discretized as one long heterogeneous cable into a large number of nodes and elements with all of the cable mass and damping lumped onto nodes; several nodes have additional mass and damping assigned due to the presence of massive system components. The differential equations of motion for the system are discretized using finite differences in space and time. The model allows for the possibility of different spatial discretizations (Δz can vary with segment), but assumes a constant time step Δt throughout the course of the simulation.

For this kind of idealization, there is only one coordinate system running from the sinker to the surface. The sinker weight is node one and the surface buoy is node nn (where nn is not related to n, the number of different cable segments that make up the system). For convenience of notation the subscript s will be used to indicate which segment a node is on. M_s and B_s are always used to describe the properties of the massive system component at the bottom of segment s. The model is fully nonlinear and thus B_s and b_s in the difference equations below are simply notationally convenient:

$$B_s = \frac{1}{2}\rho \left(C_D\right)_s S_s, \tag{2.11}$$

$$b_s = \frac{1}{2}\rho \left(C_f\right)_s \pi d_s. \tag{2.12}$$

Also for notational convenience, the wet weight of lumped mass system components and wet weight per unit length of a segment are denoted as W_s and w_s, respectively.

In the difference approximations, u_i^j indicates the displacement of node i from the unstretched position at time step j. In this notation the differenced equilibrium equation for the sinker weight

is written as

$$\begin{aligned}\left(M_1+m_1\frac{\Delta z_1}{2}\right)\left(\frac{u_1^{j+1}-2u_1^j+u_1^{j-1}}{\Delta t^2}\right) \\ +\mu\left(B_1+b_1\frac{\Delta z_1}{2}\right)\left(\frac{u_1^{j+1}-u_1^{j-1}}{2\Delta t}\right)^2 \\ +r_1\frac{\Delta z_1}{2}\left(\frac{u_1^{j+1}-u_1^{j-1}}{2\Delta t}\right) &= EA_1^a\left(\frac{u_2^j-u_1^j}{\Delta z_1}\right)-\left(W_1+w_1\frac{\Delta z_1}{2}\right).\end{aligned} \tag{2.13}$$

For a subsurface component at node i between segments $s-1$ and s,

$$\begin{aligned}\left(M_s+m_s\frac{\Delta z_s}{2}+m_{s-1}\frac{\Delta z_{s-1}}{2}\right)\left(\frac{u_i^{j+1}-2u_i^j+u_i^{j-1}}{\Delta t^2}\right) \\ +\mu\left(B_s+b_s\frac{\Delta z_s}{2}+b_{s-1}\frac{\Delta z_{s-1}}{2}\right)\left(\frac{u_i^{j+1}-u_i^{j-1}}{2\Delta t}\right)^2 \\ +\left(r_s\frac{\Delta z_s}{2}+r_{s-1}\frac{\Delta z_{s-1}}{2}\right)\left(\frac{u_i^{j+1}-u_i^{j-1}}{2\Delta t}\right) &= EA_s^a\left(\frac{u_{i+1}^j-u_i^j}{\Delta z_s}\right) \\ &\quad -EA_{s-1}^b\left(\frac{u_i^j-u_{i-1}^j}{\Delta z_{s-1}}\right) \\ &\quad -\left(W_s+w_s\frac{\Delta z_s}{2}+w_{s-1}\frac{\Delta z_{s-1}}{2}\right).\end{aligned} \tag{2.14}$$

At the surface buoy, the equilibrium condition is

$$\begin{aligned}\left(M_B+m_n\frac{\Delta z_n}{2}\right)\left(\frac{u_{nn}^{j+1}-2u_{nn}^j+u_{nn}^{j-1}}{\Delta t^2}\right) \\ +\mu\left(B_B+b_n\frac{\Delta z_n}{2}\right)\left(\frac{u_{nn}^{j+1}-u_{nn}^{j-1}}{2\Delta t}\right)^2 \\ \left(B_w^j+r_n\frac{\Delta z_n}{2}\right)\left(\frac{u_{nn}^{j+1}-u_{nn}^{j-1}}{2\Delta t}\right) &= -EA_n^b\left(\frac{u_{nn}^j-u_{nn-1}^j}{\Delta z_1}\right)+F_w^j \\ &\quad -\left(W_B+w_n\frac{\Delta z_n}{2}\right).\end{aligned} \tag{2.15}$$

Finally, for any plain nodal point along any of the cable segments,

$$
\begin{aligned}
& m_s \Delta z_s \left(\frac{u_i^{j+1} - 2u_i^j + u_i^{j-1}}{\Delta t^2} \right) \\
& \quad + \mu b_s \Delta z_s \left(\frac{u_i^{j+1} - u_i^{j-1}}{2\Delta t} \right)^2 \\
& \quad + r_s \Delta z_s \left(\frac{u_i^{j+1} - u_i^{j-1}}{2\Delta t} \right) \quad = \quad EA_s^a \left(\frac{u_{i+1}^j - u_i^j}{\Delta z_s} \right) - EA_s^b \left(\frac{u_i^j - u_{i-1}^j}{\Delta z_s} \right) - w_s \Delta z_s .
\end{aligned}
\tag{2.16}
$$

μ is a constant used to fix the sign of the quadratic drag terms because the drag force is really of the form $D \sim \dot{u}|\dot{u}|$,

$$
\mu = \begin{cases} +1, & \text{when } u_i^j > u_i^{j-1} \\ -1, & \text{when } u_i^j < u_i^{j-1} \end{cases}
\tag{2.17}
$$

F_w^j is the wave exciting force on the surface buoy and B_w^j is the coefficient of linear wave damping at time step j.

The EA terms are superscripted either with an a (above) are a b (below) to account for the the possibility that a cable can go slack when it is under zero tension. When the spatial gradient of the motion is positive above or below a node then the tension is positive and $EA_s^{a/b} = EA_s$. If the gradient is negative, the axial stiffness of the cable above or below that node is set to zero, $EA_s^{a/b} = 0$. Mathematically, these conditions are formulated as

$$
EA_s^a = \begin{cases} EA_s, & \text{when } u_{i+1}^j > u_i^j \\ 0, & \text{when } u_{i+1}^j < u_i^j \end{cases}
\tag{2.18}
$$

$$
EA_s^b = \begin{cases} EA_s, & \text{when } u_i^j > u_{i-1}^j \\ 0, & \text{when } u_i^j < u_{i-1}^j \end{cases}
\tag{2.19}
$$

Given an initial displacement at time $t = 0$ and time $t = -\Delta t$ (time steps 0 and -1) for all of the nodes (generally taken as the static equilibrium position of all the nodes when the system is in water), the motion at time step 1 is calculated by rearranging the difference equations of motion into nn quadratic equations in u_i^1 and solving each equation explicitly. Generally, at any time step, j, the motions at time step $j+1$ are computed by solving nn independent quadratic equations. For each of the four types of difference equations given above, the solutions to the quadratic equations are written as

$$
u_i^{j+1} = \frac{-c_2 + \sqrt{c_2^2 - 4c_1c_3}}{c_2},
\tag{2.20}
$$

where for the sinker

$$
\begin{aligned}
c_1 &= \frac{\mu}{4\Delta t^2}\left(B_1 + b_1\frac{\Delta z_1}{2}\right), \qquad (2.21)\\
c_2 &= \left(\frac{M_1 + m_1\frac{\Delta z_1}{2}}{\Delta t^2}\right) - \frac{\mu}{2\Delta t^2}\left(B_1 + b_1\frac{\Delta z_1}{2}\right)u_1^{j-1} + \frac{r_1}{4\Delta t}\Delta z_1,\\
c_3 &= \left[\frac{EA_1^a}{\Delta z_1} - 2\left(\frac{M_1 + m_1\frac{\Delta z_1}{2}}{\Delta t^2}\right)\right]u_1^j + \left[\left(\frac{M_1 + m_1\frac{\Delta z_1}{2}}{\Delta t^2}\right) - \frac{r_1}{4\Delta t}\Delta z_1\right]u_1^{j-1}\\
&\quad -\frac{EA_1^a}{\Delta z_1}u_2^j + \frac{\mu}{4\Delta t^2}\left(B_1 + b_1\frac{\Delta z_1}{2}\right)\left(u_1^{j-1}\right)^2 + \left(W_1 + w_1\frac{\Delta z_1}{2}\right),
\end{aligned}
$$

for a system component between cable segments

$$
\begin{aligned}
c_1 &= \frac{\mu}{4\Delta t^2}\left(B_s + b_s\frac{\Delta z_s}{2} + b_{s-1}\frac{\Delta z_{s-1}}{2}\right), \qquad (2.22)\\
c_2 &= \left(\frac{M_s + m_s\frac{\Delta z_s}{2} + m_{s-1}\frac{\Delta z_{s-1}}{2}}{\Delta t^2}\right) + \left(\frac{r_s\frac{\Delta z_s}{2} + r_{s-1}\frac{\Delta z_{s-1}}{2}}{2\Delta t}\right)\\
&\quad -\frac{\mu}{2\Delta t^2}\left(B_s + b_s\frac{\Delta z_s}{2} + b_{s-1}\frac{\Delta z_{s-1}}{2}\right)u_i^{j-1},\\
c_3 &= \left[\frac{EA_s^a}{\Delta z_s} + \frac{EA_{s-1}^b}{\Delta z_{s-1}} - 2\left(\frac{M_s + m_s\frac{\Delta z_s}{2} + m_{s-1}\frac{\Delta z_{s-1}}{2}}{\Delta t^2}\right)\right]u_i^j - \frac{EA_s^a}{\Delta z_s}u_{i+1}^j - \frac{EA_{s-1}^b}{\Delta z_{s-1}}u_{i-1}^j\\
&\quad + \left[\left(\frac{M_s + m_s\frac{\Delta z_s}{2} + m_{s-1}\frac{\Delta z_{s-1}}{2}}{\Delta t^2}\right) - \left(\frac{r_s\frac{\Delta z_s}{2} + r_{s-1}\frac{\Delta z_{s-1}}{2}}{2\Delta t}\right)\right]u_i^{j-1}\\
&\quad + \frac{\mu}{4\Delta t^2}\left(B_s + b_s\frac{\Delta z_s}{2} + b_{s-1}\frac{\Delta z_{s-1}}{2}\right)\left(u_i^{j-1}\right)^2 + \left(W_s + w_s\frac{\Delta z_s}{2} + w_{s-1}\frac{\Delta z_{s-1}}{2}\right),
\end{aligned}
$$

for the surface buoy

$$
\begin{aligned}
c_1 &= \frac{\mu}{4\Delta t^2}\left(B_B + b_n\frac{\Delta z_n}{2}\right), \qquad (2.23)\\
c_2 &= \left(\frac{M_B + m_n\frac{\Delta z_n}{2}}{\Delta t^2}\right) - \frac{\mu}{2\Delta t^2}\left(B_B + b_n\frac{\Delta z_n}{2}\right)u_{nn}^{j-1} + \frac{r_n}{4\Delta t}\Delta z_n,\\
c_3 &= \left[\frac{EA_n^b}{\Delta z_n} + \rho g A_{\text{wp}} - 2\left(\frac{M_B + m_n\frac{\Delta z_n}{2}}{\Delta t^2}\right)\right]u_{nn}^j + \left[\left(\frac{M_B + m_n\frac{\Delta z_n}{2}}{\Delta t^2}\right) - \frac{r_n}{4\Delta t}\Delta z_n\right]u_{nn}^{j-1}\\
&\quad -\frac{EA_n^b}{\Delta z_n}u_{nn-1}^j + \frac{\mu}{4\Delta t^2}\left(B_B + b_n\frac{\Delta z_n}{2}\right)\left(u_{nn}^{j-1}\right)^2 + \left(W_B + w_n\frac{\Delta z_n}{2}\right) - F_B^j,
\end{aligned}
$$

and for a regular nodal point, i, along segment s

$$
\begin{aligned}
c_1 &= \frac{\mu}{4\Delta t^2} b_s \Delta z_s, \\
c_2 &= \frac{m_s \Delta z_s}{\Delta t^2} - \frac{\mu}{2\Delta t^2} b_s \Delta z_s u_i^{j-1} + \frac{r_s \Delta z_s}{2\Delta t}, \\
c_3 &= \left(\frac{EA_s^a + EA_s^b}{\Delta z_s} - \frac{2 m_s \Delta z_s}{\Delta t^2} \right) u_i^j - \frac{EA_s^a}{\Delta z_s} u_{i+1}^j - \frac{EA_s^b}{\Delta z_s} u_{i-1}^j \\
&\quad + \left(\frac{m_s \Delta z_s}{\Delta t^2} - \frac{r_s \Delta z_s}{2\Delta t} \right) u_i^{j-1} + \frac{\mu}{4\Delta t^2} b_s \Delta z_s \left(u_i^{j-1} \right)^2 + w_s \Delta z_s.
\end{aligned}
\tag{2.24}
$$

2.3 Wave forcing

In considering possible configurations for the SSAR two possible types of surface buoys need to be considered. The first possibility is the short, squat cylindrical surlyn foam buoy currently in use on the SSARs; the second possibility is a spar buoy.

2.3.1 Wave following buoy

Frequency domain simplification

For the initial SSAR designs, it is possible to treat the surface buoy as a perfect wave follower and thus simply use wave motion instead of wave force as the system input. The underlying assumption in such a simplification is that the interaction between the surface buoy and the hose below the buoy does not play a role in the first natural mode of the system and that it is this first mode which is preferentially excited by surface waves. The higher frequency modes in which the surface buoy dynamics do play a role can be ignored because of the lack of higher frequency input energy in a typical sea spectrum. This approach saves having to develop a model of the wave exciting force, damping, and added mass for the surface buoy. With this approach, a harmonic solution for U_B is specified with a known $\hat{U}_B$; the last equation in the linear system (equation 2.8) is no longer needed and the $2n^{\text{th}}$ equation simply becomes

$$\hat{U}_B = C_{2n-1} \cos kL_n + C_{2n} \sin kL_n.$$

Time domain simplification

Like the frequency domain model, the development of a model of wave forcing can be avoided by assuming that the surface buoy is a perfect wave follower and simply specifying surface wave motion as the model input. In this case, there is no need to solve for u_{nn}^{j+1}; it is specified based on the wave

record.

The wave record is constructed from a random sea spectrum for a given sea state by breaking the spectrum into a summation of individual frequency components with separate amplitudes and random phases [3]. For example, a Bretschneider spectrum, specified with a modal frequency, ω_m, and significant height, H_s,

$$S(\omega) = \frac{1.25}{4}\frac{\omega_m^4}{\omega^5}H_s^2 e^{-1.25(\frac{\omega_m}{\omega})^4}. \tag{2.25}$$

can be discretized over a range of frequencies, ω_i, with a spacing of $\Delta\omega$. The amplitude of the i^{th} component is

$$A_i = \sqrt{2S(\omega_i)\Delta\omega}. \tag{2.26}$$

The total wave amplitude at the buoy is the sum of all the discrete wave components

$$A_B^j = \sum_{i=1}^{N} A_i \sin(j\omega_i \Delta t + t_0 + \phi_i). \tag{2.27}$$

t_0 is a constant chosen such that $A_B^0 = 0$ at $t = 0$; this is to minimize the transient effects that would result from a sudden sharp change in the buoy position at model start-up. The random phases, ϕ_i, are generated as uniform random numbers on the interval $[-\pi, \pi]$. The update equation for the actual motion of the buoy is simply

$$u_{nn}^{j+1} = A_B^{j+1} + u_{nn}^0. \tag{2.28}$$

2.3.2 Spar buoy

Frequency domain solution

Because the entire motivation for considering a spar buoy is that it does not follow the waves (in fact its motions will be substantially smaller than the surface waves), the simple wave follower assumption cannot be applied for model systems with a spar buoy. Instead, a model for the interaction between surface waves and the motions of the spar buoy, and between the motions of the spar buoy and the SSAR components hanging below it, must be developed.

Newman [15] provides a convenient derivation for the linearized equations of motion (heave, pitch, and surge) for a freely floating spar buoy with harmonic forcing. This derivation can be modified to include the effects of the tension members hanging below the buoy. For the free floating

spar buoy, the equations of motions are

$$m\ddot{\zeta} + \frac{1}{2}\frac{\omega m^2 k}{\rho \chi^2 H^2}\dot{\zeta}\left[1 - Q_0(k)\chi kH\right]^2 + \rho g S(0)\zeta = i\rho g S(0) A e^{i\omega t}\left[1 - \chi kH Q_0(k)\right], \tag{2.29}$$

$$2\ddot{\xi} + P_1\ddot{\psi} + \frac{1}{2}\frac{\omega m^2 k^3}{\rho}Q_0(k)\left[\dot{\xi}Q_0(k) + \dot{\psi}Q_1(k)\right] = 2\omega^2 A e^{i\omega t}Q_0(k), \tag{2.30}$$

$$\left({K_y}^2 + P_2\right)\ddot{\psi} + P_1\ddot{\xi} + \frac{1}{2}\frac{\omega m^2 k^3}{\rho}Q_1(k)\left[\dot{\xi}Q_0(k) + \dot{\psi}Q_1(k)\right] + gP_1\psi = 2\omega^2 A e^{i\omega t}Q_1(k). \tag{2.31}$$

ζ, ψ, and ξ are the heave, pitch, and surge, respectively. ${K_y}^2$ is the radius of gyration of the buoy. H is the buoy draft. k and ω are the wavenumber and frequency of the harmonic input, respectively. $S(z)$ is the buoy cross-sectional area as a function of depth, with $z = 0$ at the mean free surface and $z = -H$ at the bottom of the buoy. χ is the vertical prismatic coefficient,

$$\chi = \frac{m}{\rho H S(0)}. \tag{2.32}$$

P_n and $Q_n(k)$ are constants defined as

$$P_n = \frac{\rho}{m}\int_{-H}^{0}(z - z_G)^n S(z)dz, \tag{2.33}$$

$$Q_n(k) = \frac{\rho}{m}\int_{-H}^{0}e^{kz}(z - z_G)^n S(z)dz, \tag{2.34}$$

where z_G is the vertical coordinate of the center of gravity. The assumptions made in deriving these equations are that the radius at $z = -H$ is zero, the slope of the cylinder sides is slowly varying and continuous, and that the radius is small compared to the wavelength of incident waves. Equations 2.33 and 2.34 can be evaluated analytically for $S(z)$ defined in a piecewise linear fashion (Appendix A).

To modify these equations for the SSAR model the vertical tension force from the cable below the buoy must be incorporated into the heave and pitch equations. In the pitch equation, this requires that the tension be linearized about its static value by dropping the harmonically varying moment caused by the dynamic tension. That dynamic tensions are small for a SSAR with a spar buoy is a reasonable assumption given the significantly lower wave-induced motions associated with a spar buoy. Recognizing that $U_B = \zeta$ and proposing harmonic solutions for pitch and surge of the form

$$\psi = \hat{\psi}e^{i\omega t}, \tag{2.35}$$

$$\xi = \hat{\xi}e^{i\omega t}, \tag{2.36}$$

the last equation in the linear system becomes

$$i\rho g S(0) A \left[1 - \chi k H Q_0(k)\right] = -C_{2n-1} E A k_n \sin kL_n + C_{2n} E A k_n \cos kL_n$$
$$+\hat{U}_B \left[-\omega^2 M_n + i\omega B_n + \frac{1}{2}\frac{\omega m^2 k}{\rho \chi^2 H^2}\dot{\zeta}\left[1 - Q_0(k)\chi k H\right]^2 + \rho g S(0)\right]. \tag{2.37}$$

and an independent 2×2 system of equations for pitch and surge is added to the problem

$$\left[-P_1 + \frac{1}{2}\frac{im^2k^3}{\rho} Q_0(k) Q_1(k)\right]\hat{\psi} + \left[-2 + \frac{1}{2}\frac{im^2k^3}{\rho} {Q_0}^2(k)\right]\hat{\xi} = 2Q_0 A, \tag{2.38}$$

$$\left[-\left({K_y}^2 + P_2\right) + \frac{1}{2}\frac{im^2k^3}{\rho} {Q_1}^2(k) + \frac{P_1}{k} + T_0\left|H - z_G\right|\right]\hat{\psi} \tag{2.39}$$
$$+\left[-P_1 + \frac{1}{2}\frac{im^2k^3}{\rho} Q_0(k) Q_1(k)\right]\hat{\xi} = 2Q_1 A.$$

Time domain solution

Because the coefficients derived above for the frequency domain solution are difficult to apply in the time domain[1] the time domain model uses Froude-Krylov theory and the Haskind relations to calculate wave exciting and damping forces [16]. Using a slender body approximation,

$$\frac{d}{H} = O(\epsilon), \tag{2.40}$$

hydrodynamic force terms only up to order ϵ^2 are retained. This approach neglects the $O(\epsilon^4 \log \epsilon)$ added mass, damping, and exciting force contributions that come from the body scattering potential.

The Froude-Krylov component of the exciting force is obtained by integrating the pressure field of the incident wave over the surface of the spar buoy,

$$F(t) = \int_{-H}^{0} \frac{dS}{dz} p(z,t) dz. \tag{2.41}$$

Assuming linear incident waves and a linearized form of Bernoulli's equation, the pressure can be written as

$$p(z,t) = \rho g A e^{kz} \sin \omega t, \tag{2.42}$$

[1]Simple superposition does not apply because the time domain model never comes to a true steady-state and thus the result at each discrete frequency is not simply the regular wave solution.

and equation 2.41 becomes

$$F(t) = \rho g A \sin\omega t \left[S(0) - S(-H)e^{-kH} - k \int_{-H}^{0} S(z) e^{kz} dz \right]. \tag{2.43}$$

Horizontal variations in pressure are neglected because d is small with respect to the incident wavelength. If the incoming wave field is given by equation 2.27, then the total exciting force at time step j is

$$F_w^j = \sum_{i=1}^{N} \left(F_w^j\right)_i, \tag{2.44}$$

where

$$\left(F_w^j\right)_i = \rho g A_i \sin\left(j\omega_i \Delta t + t_0 + \phi_i\right) \left[S(0) - S(-H)e^{-k_i H} - k_i \int_{-H}^{0} S(z) e^{k_i z} dz \right]. \tag{2.45}$$

Like the integral for the P and Q coefficients in the frequency domain model, the integral in this equation can easily be evaluated analytically for $S(z)$ piecewise linear.

To prevent an uncontrolled resonance from the contributions with frequencies near the natural frequency of the spar buoy, an $O(\epsilon^4)$ approximate damping term is reintroduced using the Haskind relations [16]. For a three-dimensional axisymmetric body, the wave damping reduces to

$$B_w^j = \sum_{i=1}^{N} \frac{k_i}{4\rho g V_g^i} \left| \left(F_w^j\right)_i \right|^2. \tag{2.46}$$

2.4 Model validation

2.4.1 Wave follower assumption

In order to test the validity of the assumption that the standard SSAR surface buoy is a wave follower, two different types of frequency domain comparisons were performed. In the first comparison, the transfer function for subsurface case motion was calculated assuming unit amplitude motion input (the wave follower assumption). This result was compared to a transfer function computed using the wave forcing model, with surface buoy exciting force, damping, and added mass coefficients computed using a numerical technique [8]. The two transfer functions are shown in the left panel of figure 2-2. The most obvious difference is the divergence after about 0.6 Hz. This difference is a result of the mode represented by the spring-like buoyancy restoring force at the buoy that is not present in the model using the wave following assumption. Models using the wave follower assumption are essentially neglecting any energy that enters the system through this mode (or that

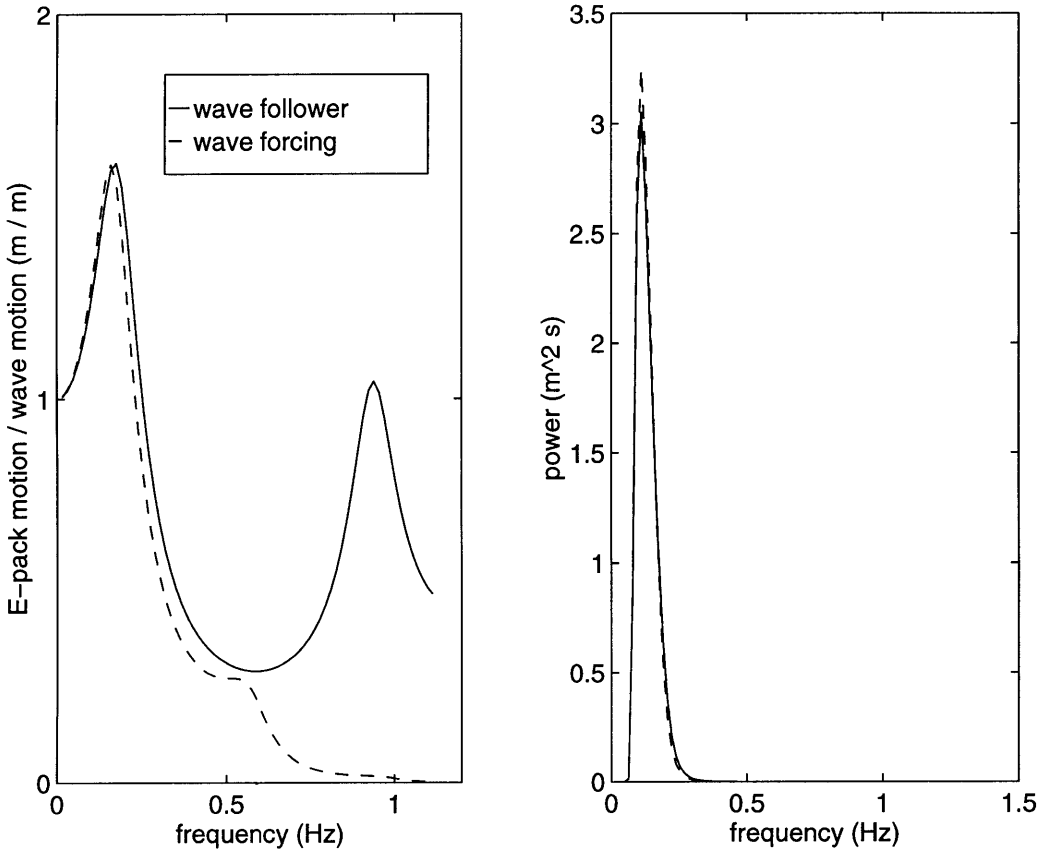

Figure 2-2: Comparison of model results for frequency domain calculations using the wave following assumption and wave forcing coefficients for a baseline SSAR configuration. The left panel shows the transfer function between surface wave amplitude and subsurface case acceleration. The right panel shows the output spectra of subsurface case acceleration given a Bretschneider spectrum (significant height 3.6 m, peak period 9.7 seconds) as input at the surface.

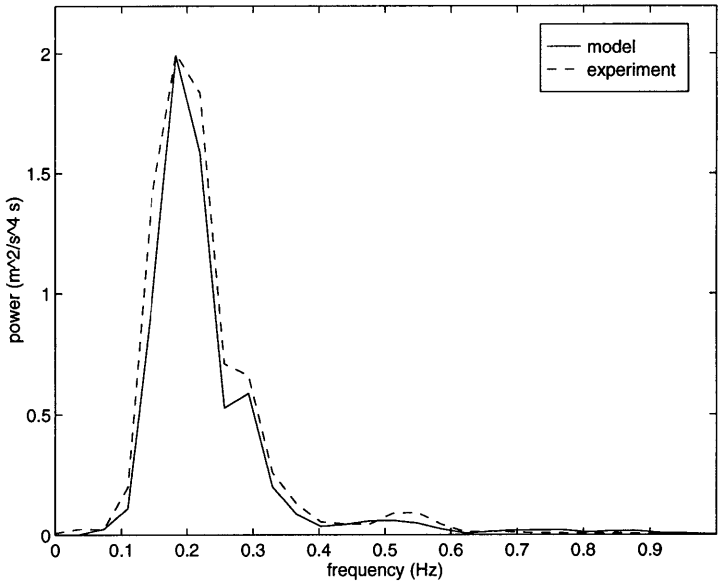

Figure 2-3: Modeled and experimental output spectra for acceleration of the subsurface case in the system with extra sinker weight.

is removed via the damping in this mode). The peak at the 1.7 second period (roughly equal to the heave natural frequency of the surface buoy) for this mode is approaching the high frequency limit of the input wave energy.

To further quantify the error introduced by the wave follower assumption, output spectra for the above two cases were also computed. The output spectra are shown in the right panel of figure 2-2. Because the two transfer functions showed substantial agreement over low frequencies, the two output spectra are nearly identical. The large divergence observed in the transfer functions after 0.6 Hz is not present in the output spectra because there is very little wave energy in the input spectrum at those higher frequencies.

2.4.2 Frequency domain output spectra

A comparison of frequency domain model results and spectral data from at sea accelerometer records is shown in figure 2-3. To make the comparison, the vertical motion of the surface buoy during the experiment was calculated by integrating the accelerations recorded by the vertical axis of a three-axis accelerometer that was located in the surface buoy. Then, a motion spectrum was computed using an 8192 point Hanning window over the 36000 point time series. Next, a model transfer function between surface motion and subsurface case acceleration was computed on the

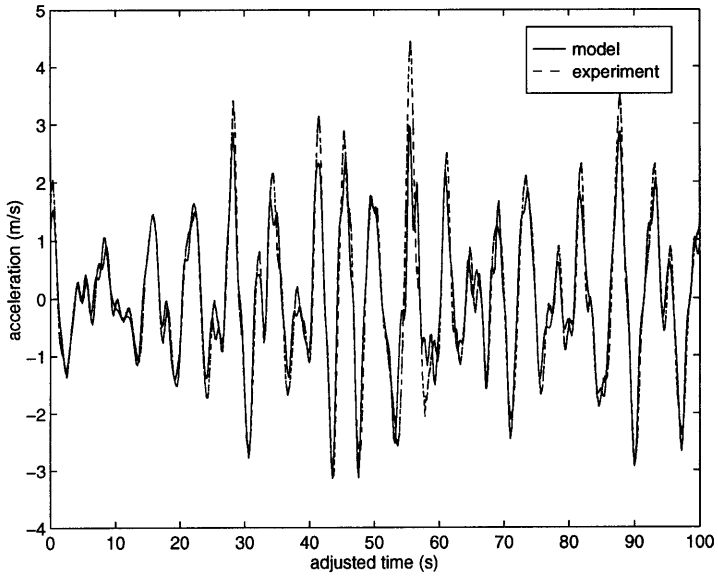

Figure 2-4: Comparison of accelerometer data from at-sea tests with model results generated by forcing the system with the actual surface motion from the at-sea test.

same frequency grid as the spectrum of experimental surface motion. The motion spectrum was multiplied by the square of the modeled transfer function. The resulting model output spectrum for pressure case acceleration can be compared to an acceleration spectrum that was computed from the acceleration time series recorded by a single axis (vertically aligned) accelerometer located within the subsurface case during the experiment.

The comparison is quite good across the 0 – 1 Hz region. The observed and predicted natural frequencies are the same to within the 0.03 Hz resolution of the FFT. The model result is slightly smaller than the experimental data over most frequencies, suggesting that the linearized damping model in the frequency domain calculation underestimates the actual level of damping in the system. The comparison can only be accurate to within the limits of the wave follower assumption because the wave follower assumption is implicit in the treatment of the integrated surface buoy accelerations as the record of surface wave motions.

2.4.3 Time domain acceleration results

The time domain model was validated by comparing the result of a numerical experiment that used the integrated surface motions discussed above as input and the actual motions of the subsurface components recorded during that sea trial. The result is shown in figure 2-4. After eliminating the

	Position		Velocity		Acceleration	
	freq	time	freq	time	freq	time
pressure case	0.0827	0.0802	0.0555	0.0532	0.0389	0.0387
subsurface float	0.0812	0.0788	0.0544	0.0521	0.0380	0.0377
spar buoy	0.0616	0.0604	0.0403	0.0377	0.0275	0.0263

Table 2.1: Standard deviation of motion variables for time and frequency domain models using a spar buoy given the same spectrum as input. Units are m (position), m/s (velocity) and m/s^2 (acceleration).

start-up transients from the numerical computation, the results appear to be nearly identical. The only obvious errors in the numerical result are some reduction in the overall magnitude of some of the highest acceleration peaks and some overshoot in a few others.

2.4.4 Comparison of time and frequency domain spar buoy results

In order to validate the simplifications made in the time domain model for the spar buoy against the more rigorously derived frequency domain model, statistical results from both models given the same Bretschneider spectrum as input were compared. For a sea state 4 (significant height 2.1 m, peak period 7.7 seconds) and a 100 second time series from the time domain model, the results in terms of standard deviations are shown in table 2.1.

The very close agreement between the two models indicates the closeness between the frequency- and time-domain derivation of forcing. The forcing in both models is based on a Froude-Krylov type pressure integration. Much of the added complexity of the frequency domain model comes from the incorporation of pitch and surge. The damping in the frequency domain is more rigorously derived, but the Haskind approximation provides an adequate approximation in the time domain. Any error in the damping in either model would be difficult to discern because of the fourth-order dependence.

2.4.5 Damping coefficients

Bluff body and skin friction drag coefficients (C_D and C_f) were determined from published values for components that are similar to those used on the SSAR [2]. The structural damping coefficient for the snubber hose was determined experimentally. A hose was suspended from a crane (in air) and instrumented with accelerometers at the top and bottom flanges. A hammer was then used to impulsively excite the system at the top flange. The damping coefficient in a frequency domain model of this simple system was then manipulated until the model transfer function matched the transfer function derived from the spectra of the two accelerometer records.

Early model results did not have any structural damping in the electromechanical cable. After reviewing the results from initial sea trials, it was clear that by neglecting damping in the cable the models were overestimating the effect that a snap in the hose could have on the subsurface components (subsurface pressure case and array elements). In subsequent models, the structural damping constant was increased to its maximum reasonable value to provide as much filtering of snap events as possible. Reasonable in this case refers to a damping level that keeps the model results in line with observed experimental values. Unfortunately, the structural damping could not be increased to a point where the snap effects were completely eliminated at the pressure case and still maintain the proper level of pressure case motions. For this reason, time-domain model acceleration results that are presented in subsequent chapters have had an additional low-pass filter applied as a post-processing step. This filter is applied only when it is clear that the snap events were in the hose and not in the electromechanical or array cables themselves.

Chapter 3

Experimental Identification of Noise Sources

3.1 Noise in an array mounted hydrophone

The data from the initial sea trials can provide a basic relationship between velocity and noise for a hydrophone that is mounted on the array cable. Figure 3-1 shows the hydrophone noise power versus velocity and frequency for the SSAR system with extra sinker weight during the September, 1995 sea trials. This plot was generated by sliding a 64 point window over the time series of the response from hydrophone one and array vertical velocity (as integrated from the vertical component of a tri-axial accelerometer mounted on the array). For each window, the mean velocity and the power spectral density of the hydrophone response in the 35 – 110 Hz band were computed. The results were binned into a velocity/frequency grid and averages were computed using the total number of results in each bin.

The acceleration-induced portion of the noise in figure 3-1 can be separated from the total noise by considering the acceleration equivalent noise power. Acceleration equivalent noise power is the signal level from the hydrophones that is due solely to accelerations in the 35 – 110 Hz frequency band. It is calculated using the signal level from the vertical axis of the tri-axial accelerometer and the known acceleration response of the hydrophones (-30 dBV re G). This result is shown in figure 3-2. Unfortunately, the accelerometer data from the sea trials is somewhat limited in that the tri-axial accelerometer had a mechanical shockmount that attenuated signals above 70 Hz and the analog front-end for the accelerometers had some filtering in it that also attenuated signals starting at about 70 Hz. The filtering is not sufficient to completely remove signals in the 70 – 110 Hz range,

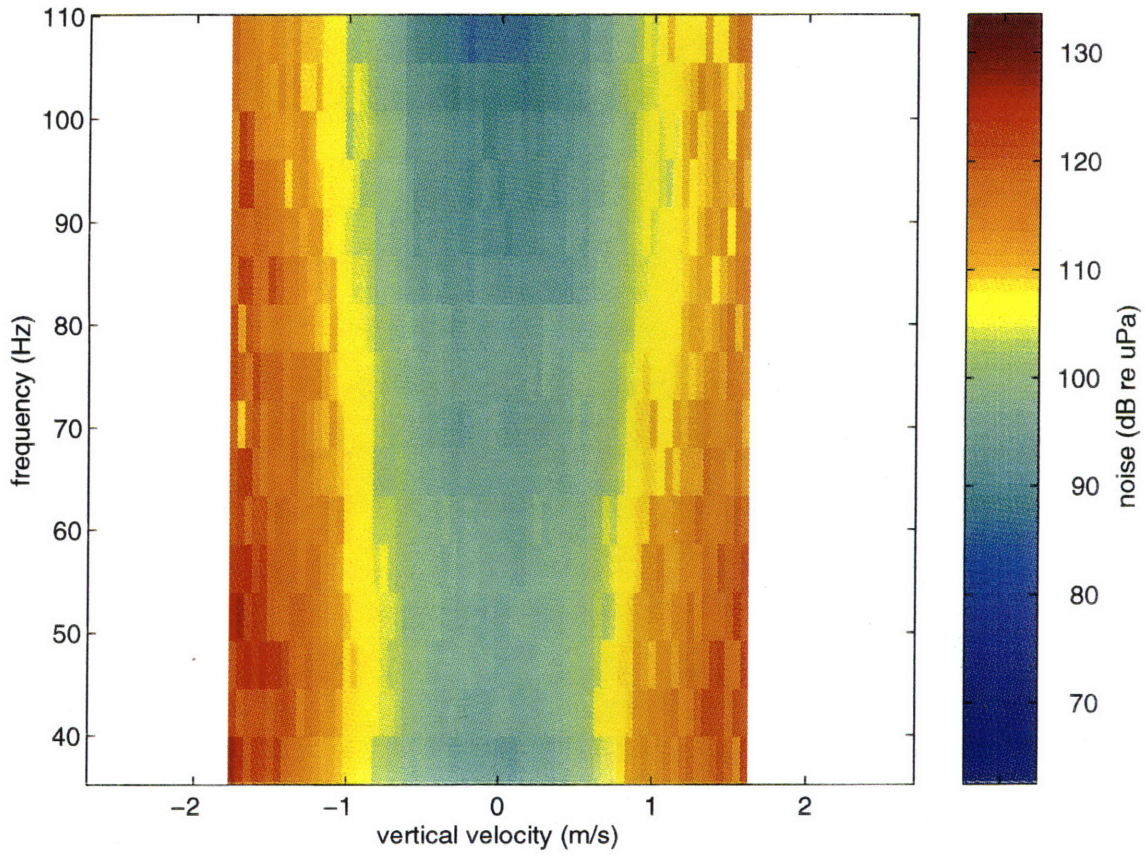

Figure 3-1: Noise in hydrophone one as a function of velocity during at sea testing of the system with extra sinker weight. Note that the color scale and horizontal axis scaling are the same for all of the color noise plots in this chapter.

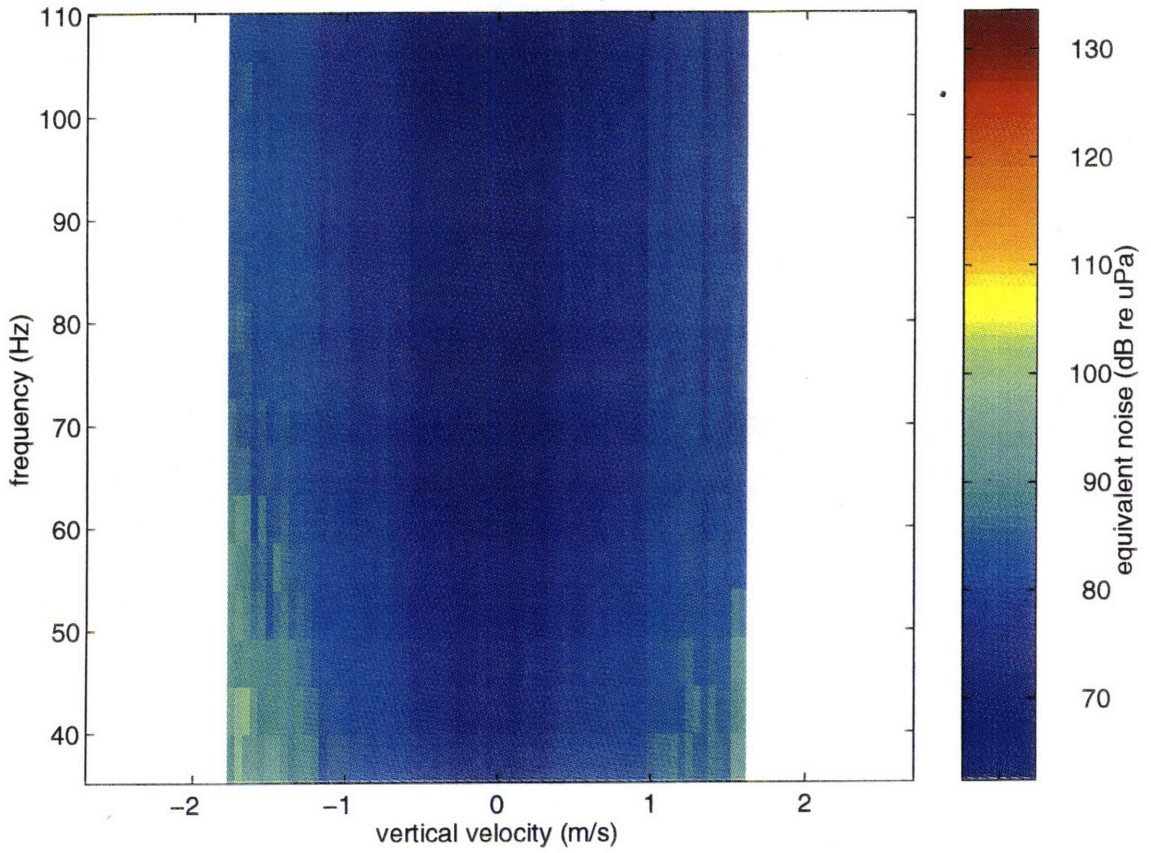

Figure 3-2: Acceleration equivalent noise as a function of velocity during at sea testing of the system with extra sinker weight.

but it may account for the reduction in equivalent noise level with frequency that is evident in the higher frequencies of figure 3-2.

The total hydrophone noise (figure 3-1) is larger than the acceleration equivalent noise (figure 3-2) across all velocities and frequencies. The total hydrophone noise represents the superposition of both acceleration-induced and flow-induced noise. That the difference at the higher velocities may be as much as 30 dB suggests that flow noise is the dominant contribution in the hydrophone noise. However, the acceleration-induced noise power alone, 90 – 100 dB at low frequencies and velocities greater than 1.5 m/s, is high enough that both noise sources need to be eliminated in order to make the SSAR functional.

Another important observation in comparing figures 3-1 and 3-2 is the performance at near zero velocity. In general, the flow noise should approach zero at very low speeds; if there is noise at low speed then the hope would be that it was acceleration- rather than flow-induced. This is clearly not the case for the unshielded, array-mounted hydrophones on the SSAR. Near zero velocity, the acceleration-induced noise of the SSAR is very low, approximately 70 dB in a band-averaged sense. This is lower than the expected 80 – 85 dB ocean ambient noise expected in the test area due to distant shipping [18]. The hydrophone noise is approximately 90 dB at near zero speeds. One possible explanation for noise even at low vertical velocities is the presence of a current. A current is capable of exciting flow noise either directly, by creating turbulence as it flows over the hydrophones, or indirectly by exciting flow-induced vibration of the array and thus causing horizontal oscillations of the hydrophones.

3.2 Noise in a flow-shielded hydrophone

3.2.1 Flow shield design

In response to the high levels of both flow- and acceleration-induced noise in the system tested during the first sea trials, a radically different array concept was proposed. The concept is to remove the array and move a single hydrophone into a large flow shield and attach the shield rigidly to the bottom of the pressure case (figure 3-3). The idea behind the new design is two-fold. One, removing the array cable eliminates the acceleration-induced noise generated locally on the array; accelerometers mounted inside the pressure case during the sea trials contained none of the high frequency acceleration signals that were evident in the array mounted accelerometers. Secondly, the flow shield provides a barrier between the irregular, turbulent flow (and resulting pressure fluctuations) and the hydrophone. At low frequencies (< 500 Hz), it is the vibration of the hydrophone wall, excited by turbulent pressure fluctuations, which is the dominant contributor to

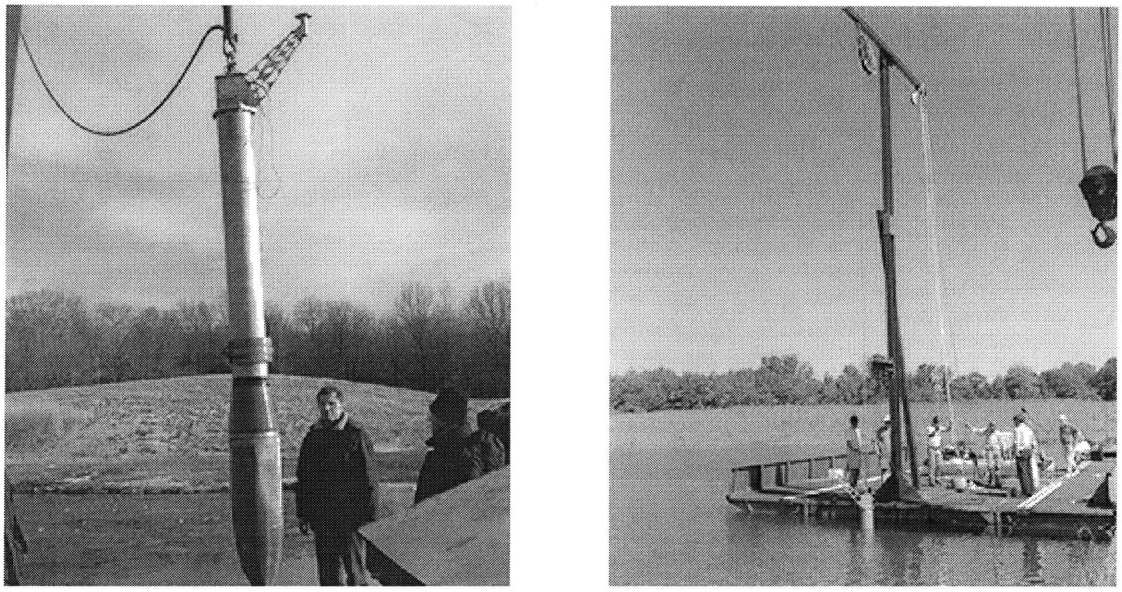

Figure 3-3: The prototype flow shield and pressure case and the test rig at the Briar Point Test Facility.

flow noise; the radiated, far-field component (i.e., the true sound), which the flow shield does not protect against, is only of secondary importance [9]. The shield consists of a wire mesh enclosure packed with open cell foam. The hydrophone is packed deep within the center of the foam, which is acoustically transparent when flooded.

3.2.2 Low ambient flow noise experiments

In order to quantify the flow noise reduction potential of the flow shield, experiments were conducted at the U.S. Army's Aberdeen Test Center (ATC) in Aberdeen, Maryland. The Underwater Explosives Test Facility (UTF) at ATC maintains an isolated pond at their Briar Point Test Site which has a very low background noise level. The tests were conducted from a barge located over the deepest (approximately 15 m) part of this pond. The test apparatus is shown in the right panel of figure 3-3. The subsurface pressure case, with a single flow-shielded hydrophone rigidly mounted to it was either pulled upwards or dropped downwards in the pond to generate flow over the hydrophone at speeds comparable to (and greater than) the velocities observed during sea trials. Tests with no motion showed an ambient noise level in the pond of approximately 72 dB re μPa across the 35 – 110 Hz band of interest. This is significantly lower than the 80 – 85 dB expected ambient noise levels in the open ocean. The low ambient noise floor allows for the quantification of noise even at

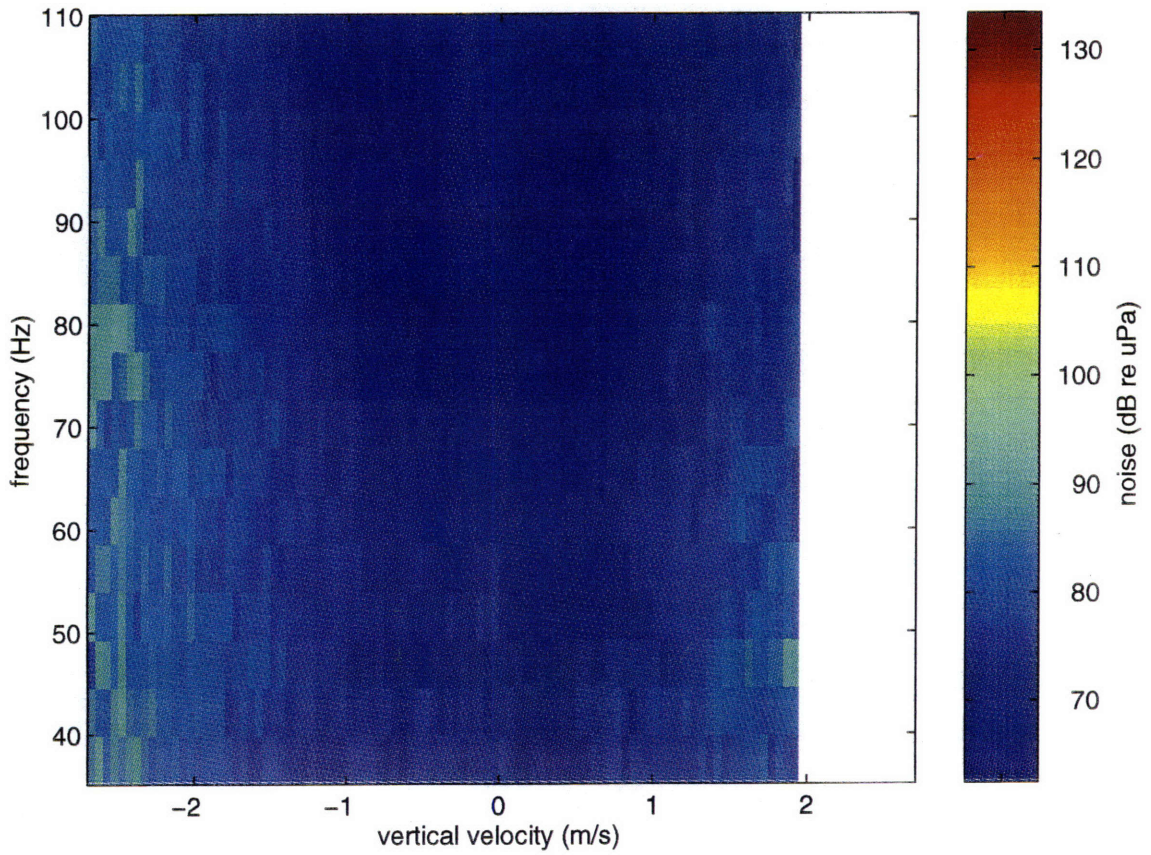

Figure 3-4: Hydrophone noise during the shielded flow noise experiments in a pond with low ambient noise.

low speeds.

Figure 3-4 shows the hydrophone noise for both the upwards and downwards moving tests. The noise is significantly lower than for the hydrophone mounted on the array. For a velocity of 1.0 m/s the noise in the array-mounted hydrophone is approximately 110 dB at low frequencies, and no less than 100 dB at high frequencies. At the same speed, the flow-shielded hydrophone has a noise level of less than 80 dB for all frequencies, with levels approaching the 72 dB ambient at high frequencies.

3.2.3 Sea trial results

The single flow-shielded hydrophone design was sea tested in March, 1997. Figure 3-5 shows the hydrophone noise recorded during the trials as a function of velocity and frequency. The maximum noise is a peak at about 50 Hz that increases to approximately 100 dB at upward velocities of

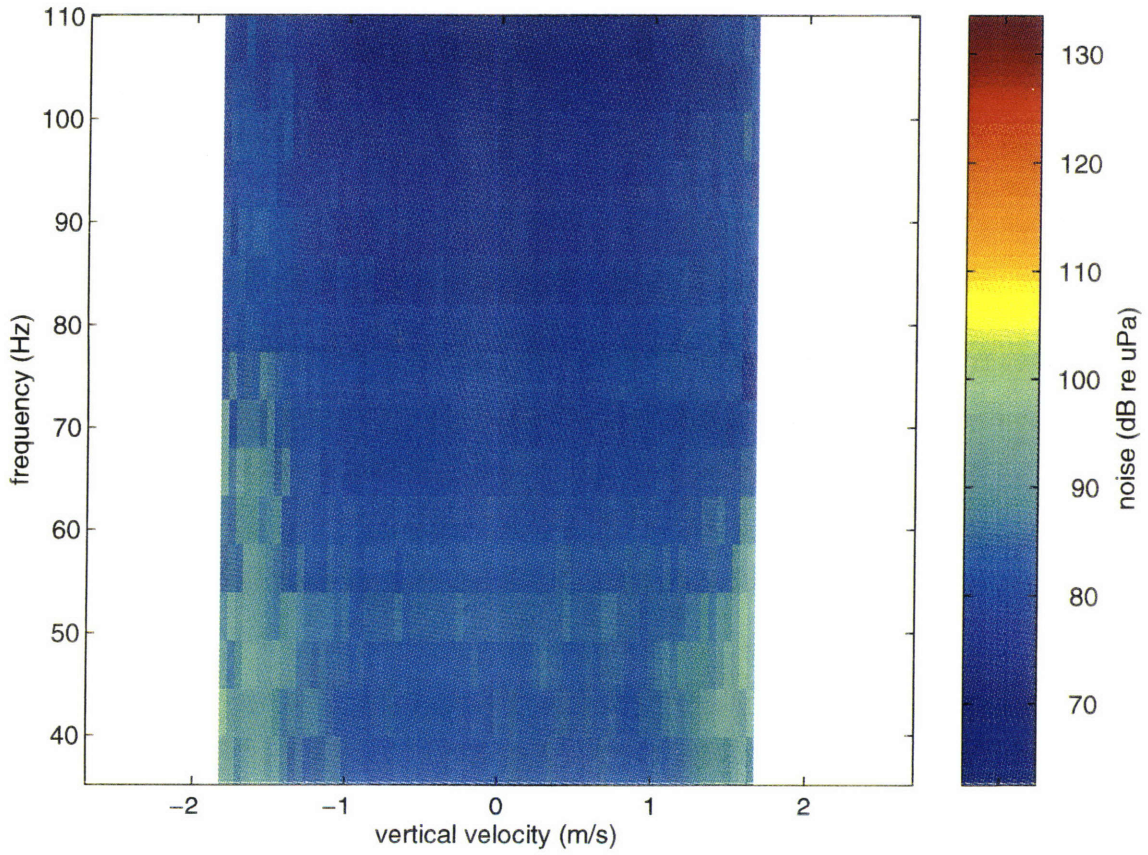

Figure 3-5: Hydrophone noise during the at-sea tests with a shielded hydrophone.

1.5 m/s. This compares to a noise level of approximately 120 dB across a broader frequency band at the same speeds for the array-mounted hydrophone (figure 3-1). It is not as low as the noise level recorded during the Aberdeen test.

The flow noise from the sea trials looks qualitatively similar in shape to the noise from the Aberdeen tests (figure 3-4). The major difference between the two is a reduction in noise power over all velocities and all frequencies for the experiments conducted in the pond. This suggests that the full SSAR system, even with no array cable, still has sources of mechanical noise; sources that were not present in the system consisting just of the pressure case tested at Aberdeen. The sinusoidal nature of the motion during at-sea deployments may be responsible for creating such a source, as the resulting oscillatory inertial and hydrodynamic pressure forces on the hydrophones may have caused them to work loose within the foam. Any subsequent motion and rubbing of the hydrophones within the foam would act as a noise source. Such an effect is unlikely to have occurred during the Aberdeen tests because each run only took from five to fifteen seconds to complete and the forces were unidirectional during the run.

3.3 Noise as a function of velocity

To formulate an empirical model of noise which could be easily applied to data calculated from the numerical models detailed in chapter 2, band-averaged noise power (across the 35 – 110 Hz band) was computed at each of the velocity levels in the noise plots shown in figures 3-1, 3-2, 3-4, and 3-5. For each case, the results were then plotted on a logarithmic velocity scale and three velocity regimes were defined subjectively by eye – a flat, ambient region, a transition region, and a completely velocity dependent region. In the ambient region the noise levels were simply averaged to give a flat noise level up to the transition point. In the transition and velocity dependent regions, linear least-squares fits were made to each set of data points. The final critical velocities between the regimes were defined as the intersections of the lines fitted to each regime.

In figure 3-6, the first onset of noise above the noise minima for the unshielded hydrophone on the array occurs at 0.2 m/s; the steepest, fully velocity dependent regime begins at approximately 0.55 m/s. The very steep slope of the noise and the low speeds at which the noise begins to rise sharply is indicative of the severe noise problems in the baseline array design. The noise in this case is proportional to $V^{4.95}$, an exponent which is consistent with typical values that are reported in the literature for flow noise. Arakeri *et al* [1] cite experimental evidence to derive a fifth power of velocity dependence for flow noise at the stagnation point of an axisymmetric body. For this same case, Lauchle [13] reports that the exponent should be between 6 and 7.5. Legendre [14] uses

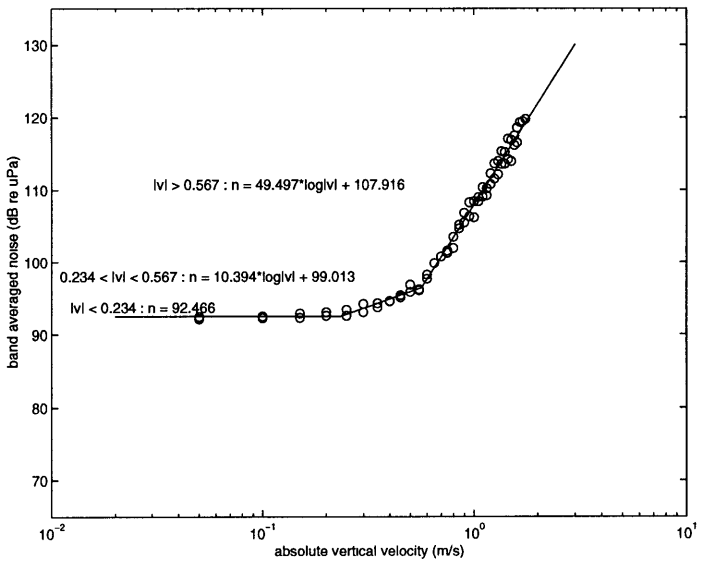

Figure 3-6: Band averaged noise model for a hydrophone attached to the SSAR array cable.

theoretical arguments to derive a sixth power dependence for the noise generated by a turbulent boundary layer. Such close agreement between the noise relationships derived for the SSAR and previous research on flow noise strongly supports the assertion that the primary noise source for the baseline array is flow noise.

Figure 3-6 and the model for acceleration-induced noise in figure 3-7 confirm the earlier observation regarding figures 3-1 and 3-2 – that the hydrophone noise even at near zero speeds is unacceptably high. This high level cannot be explained by the acceleration-induced component which is more than 20 dB lower. While the onset of acceleration-induced noise occurs at approximately the same point (0.2 m/s), the slope of the acceleration-induced noise is only half that of the flow noise.

The noise model for a single shielded hydrophone during the sea trials is shown in figure 3-8. In this case the noise near zero velocity is at a level consistent with ocean ambient. The flow shield delays the onset of noise to approximately 1.0 m/s and also reduces the slope after onset by almost a factor of two compared to the unshielded, array-mounted hydrophone.

As figure 3-7 presents a picture of pure acceleration-induced noise (or as nearly pure as possible given the current data set), figure 3-9, using the data from the Aberdeen experiments, presents as pure a picture as possible of flow-induced noise. The slopes for acceleration-induced noise (noise $\sim V^{2.51}$) and the hydrophone noise from the shielded sea trials (noise $\sim V^{2.61}$) are quite close,

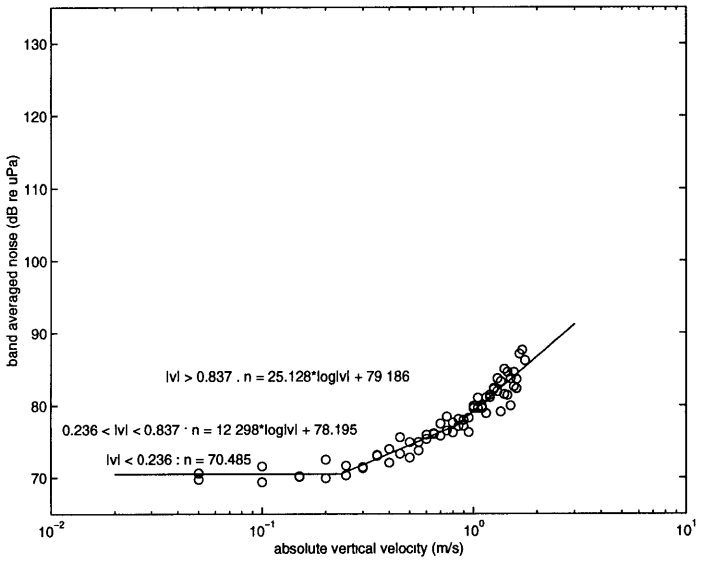

Figure 3-7: Band averaged acceleration equivalent noise model for a hydrophone attached to the SSAR array cable.

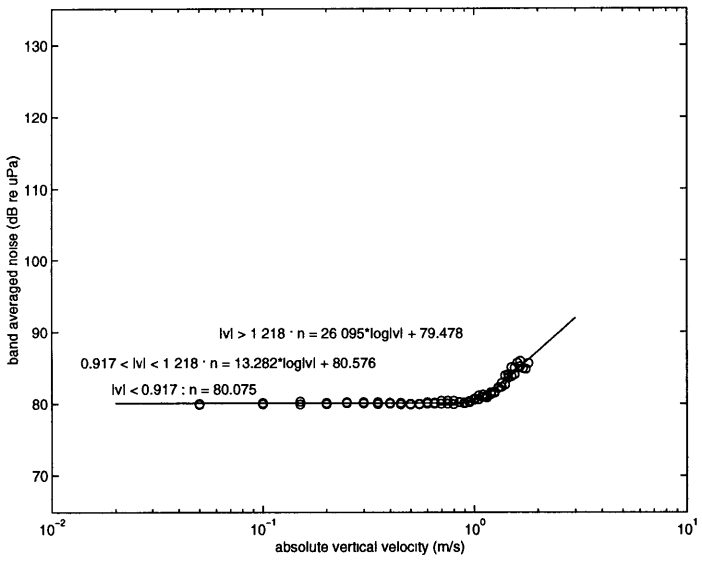

Figure 3-8: Band averaged noise model for the flow shield encased hydrophone attached to the SSAR bottom pressure case during sea trials.

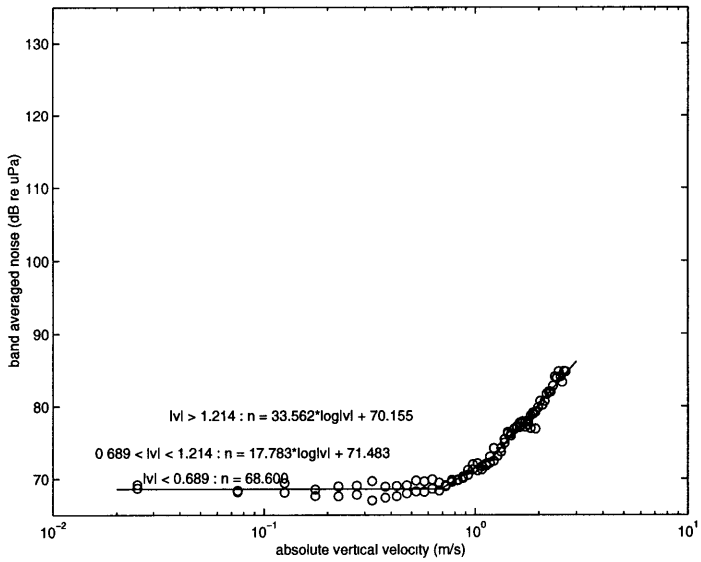

Figure 3-9: Band averaged noise model for the flow shield encased hydrophone attached to the SSAR bottom pressure case during the Aberdeen pond tests.

suggesting that there was indeed a mechanical (acceleration) noise source in the flow shield used during the March, 1997 sea trials. The slope of the flow noise from the Aberdeen tests (noise $\sim V^{3.36}$) is larger than this, but still lower than the $V^{4.95}$ of the unshielded hydrophones. This suggests that both flow and mechanical noise were present in the flow-shielded hydrophone during the Aberdeen tests, but that the mechanical noise was not large enough to be the dominant source. This situation could occur if there was a small amount of mechanical noise present along with the residual flow noise that the flow-shield did not prevent.

Chapter 4

Modeling Noise Reduction

This chapter presents results that combine the numerical model predictions of system motion with the experimentally derived relationships between velocity and hydrophone noise. The two tools can be used together to generate a table that gives the noise performance, as well as other important performance measures such as the prevalence of snap loading, for a wide variety of system configurations. For completeness, the table includes both configurations that have already been tried and discarded as unacceptable and those which are currently still being considered as possible SSAR designs.

4.1 Evaluating performance

4.1.1 Noise

When discussing the noise performance of the SSAR it is important to have a target maximum allowable noise level. The original tomographic calculations for the SSAR were based on a range of 3000 km, an ambient of 80 dB and no additional flow- or mechanically-induced noise [5]. For every six dB of noise (either ambient or self-noise), the range at which the SSAR can measure an optimal number of arrivals from the source is halved. At a cost of some accuracy, fewer numbers of arrivals can be used in the tomographic calculations.

The SSAR processes incoming acoustic signals by averaging over a ten minute time period. For this reason, modeled noise levels are computed by running a ten minute time series of modeled hydrophone velocity through the appropriate noise model (figure 3-6 or figure 3-8) and averaging the resulting noise level over that ten minute period. Sea state averaged noise levels are computed by averaging the noise level in each of sea states 2 – 8, weighting each sea state with the probabilistic

sea state	significant height (m)	peak period (s)	probability of sea state
2	0.3	6.3	6.40
3	0.88	7.5	15.50
4	1.88	8.8	31.60
5	3.25	9.7	20.94
6	5.0	12.4	15.03
7	7.5	15.0	7.00
8	11.5	16.4	1.56

Table 4.1: Parameters for each of the modeled sea states. Data is taken from the mean and most probable North Pacific values in table 2.3 of Faltinsen [3]. Sea states greater than 8 and less than 2 are not modeled; they account for a 1.37 percentage probability of occurrence.

fraction of time that it occurs over one year. Both the weighting factors and the significant heights and modal periods for each sea state are shown in table 4.1.

Once the band- and time-averaged noise level for each configuration in each sea state has been computed, the noise level can be related to the RMS hydrophone velocity calculated from the frequency domain model for the same configuration and sea state. The advantage of such a relationship is that the RMS velocity can be very quickly computed. The time domain model takes approximately 90 minutes to generate 10 minutes of simulated motion for a single configuration in a single sea state on a 200 MHz Pentium Pro computer. In contrast, the frequency domain model can compute an RMS velocity for the same configuration in the same sea state in less than three seconds.

The frequency domain model can also be used to compute the number of times per ten minute averaging period that the velocity exceeds a critical value, v_0, such as 0.5 m/s for hydrophones on an array or 1.0 m/s for a flow-shielded hydrophone. Given the spectral moments of velocity, M_0^v $(= \sigma_v)$ and M_2^v, the upcrossing rate, $n(v_0)$, in units of events per ten minutes is given by

$$n(v_0) = \frac{600}{2\pi}\sqrt{\frac{M_2^v}{M_0^v}}e^{-v_0/2M_0^v}. \tag{4.1}$$

4.1.2 Longevity and survivability

In addition to the noise performance of a given configuration, several other parameters that affect overall performance and longevity must also be considered. In each sea state the frequency domain model can be used to calculate a spectrum of tension for each configuration. Using the spectrum from the extreme sea state (sea state 8) a maximum design tension can be calculated as the static

	d (m)	m (kg/m)	E (N/m^2)	C_f	r (kg m/s)
wire rope	0.008	0.193	8.3×10^{10}	0.005	0
array	0.015	0.243	7.6×10^{9}	0.06	0
EM cable	0.013	0.320	3.0×10^{10}	0.005	0.2
hose	0.104	9.61	4.0×10^{6}	0.03	3.0

Table 4.2: Properties of the types of cable used on the SSAR.

tension plus an extreme dynamic tension [8],

$$T^{1/1000} = 3.97\sigma_T^8, \tag{4.2}$$

where σ_T^8 is the standard deviation of tension in a sea state 8 and $T^{1/1000}$ is the average of the 1/1000 highest tensions expected during such a storm. From the tension results across all the sea states, the number of expected snap events per year in each cable member can also be computed

$$n = 365 \times 24 \times 3600 \sum_{j=2}^{8} \frac{f_j}{2\pi} \sqrt{\frac{M_2^j}{M_0^j}} e^{-T_0/2M_0^j}, \tag{4.3}$$

where T_0 is the effective static tension in the member, M_2^j and M_0^j are the moments of the spectrum of tension in the member in sea state j and f_j is the fraction of time in one year that sea state j occurs (from table 4.1). Finally, because marine growth is a potential problem, the total available reserve buoyancy of each configuration will be considered.

4.2 Modeled configurations

Tables 4.2 and 4.3 lists the mechanical properties of the cables and components used in the modeled SSAR configurations. The notation matches that used in chapter 2 except where noted. Table 4.4 details the way in which the above listed components were pieced together to form each of the different model configurations.

4.2.1 Component changes

Configurations 1 – 4 are all variations of the baseline SSAR. The full 60 m array cable is present and the wave following buoy is at the surface. The first configuration is simply the baseline SSAR. The expectation is that it will be noisy and have significant numbers of snap events. Configuration 2 is the same as the baseline except for the addition of approximately 480 lbs at the sinker weight. This

	M (kg)	M_a (kg)	buoyancy (N)	S (m^2)	C_D
sinker	109	1.6	160	0.016	1.0
shackle	0.5	0.0	0.0	0.0	0
pressure case	147	9.11	1000	0.052	1.2
subsurface float	49.7	117.8	2310	0.454	0.6
flange	32.0	3.7	246	0.028	1.2

Table 4.3: Properties of the lumped mass components used on the SSAR. M is the mass of the component; M_a is the added mass of the component. $M + M_a$ equals the virtual mass used in the equations of chapter 2.

1	2	3	4	5
sinker	sinker ×3	sinker	sinker ×3	pressure case+180
wire rope	wire rope	wire rope	wire rope	EM cable
shackle	shackle	shackle	shackle	subsurface float
array	array	array	array	hose
pressure case	pressure case	pressure case	pressure case	wave follower
EM cable	EM cable	EM cable	EM cable	
subsurface float	subsurface float	flange	subsurface float	
hose	hose	hose	hose	
wave follower	wave follower	wave follower	flange	
			hose	
			wave follower	
6	7	8	9	10
pressure case +90	sinker	pressure case+90	pressure case+90	pressure case
EM cable	wire rope	EM cable	EM cable	EM cable
flange	shackle	subsurface float	subsurface float	flange
hose	array	hose	hose	hose
wave follower	pressure case	6 inch spar	8 inch spar	8 inch spar
	EM cable			
	subsurface float			
	hose			
	8 inch spar			

Table 4.4: Layout, from the bottom up, of cables and components for each of the modeled SSAR configurations. Multiplier listed after the inclusion of a sinker indicate that the mass, added mass, buoyancy and surface area were all increased by that multiple for that configuration. An additional number after the pressure case indicates an additional amount of mass (in kilograms) added inside the case.

is the configuration that was sea-tested in September, 1995, the experimental results from which the array mounted hydrophone noise model (figures 3-1 and 3-6) was generated. The idea behind the additional sinker weight is to reduce the snap loading, not to reduce the velocities. Configuration 3 is simply another way to achieve a reduction in snap loading; removing the subsurface float has about the same effect on the hose static tension as adding 410 lbs of sinker weight.

Configuration 4 presents the first attempt at reducing both snap loading and velocities. The sinker weight is increased and an additional hose is placed in series with the top snubber hose. The first mode of the wave following SSAR can be roughly computed by treating the hose as a single spring and everything below it as a single mass. If $K_{eq} \approx 1250$ N/m and $M_{eq} \approx 1000$ kg then a second hose in series would move the natural period from about 5.6 seconds to about 8 seconds and away from the region of highest wave energy in the lower sea states.

4.2.2 Single hydrophone solution

Given the goal of a noise level no greater than 80 dB it is clear from figures 3-1 and 3-2 that the performance of SSARs with an array cable is unacceptable; the noise levels in the noise model (figure 3-6) are almost constantly above 90 dB and with any significant motion quickly exceed 100 dB. Configurations 5 – 10 are designs based on removing the array and replacing it with a single flow-shielded hydrophone. Configurations 5 and 6 maintain the wave following surface buoy and configurations 8 – 10 replace the wave follower with a spar buoy. For the wave following designs, the weight that had been at the sinker must be moved up to the bottom pressure case because snap loading in the hose is still a concern. Configuration 5 retains the subsurface float and adds 400 lbs at the pressure case; configuration 6 removes the subsurface float and only adds 200 lbs at the pressure case. Configuration 6 represents the system used during the March, 1997 sea trials, from which the shielded hydrophone noise model (figure 3-8) was generated.

4.2.3 Spar buoy

The basic shape of the spar buoy used in the models is shown in figure 4-1. The design is based on maximizing the advantages provided by a spar buoy (which means maximizing draft to reduce wave exciting forces and minimizing diameter to increase the natural period of heave) while working within some practical constraints to insure that the buoys will be inexpensive, relatively easy to build and deploy, and will have sufficient reserve buoyancy. The design consists of a 12.2 m (40 ft) aluminum pipe with the 1.8 m long topside pressure case attached to the bottom. The 40 ft length was chosen as a compromise between performance and ease of assembly, shipping (it will fit inside a standard shipping container) and at sea deployment. There is a surlyn wrap around the pressure

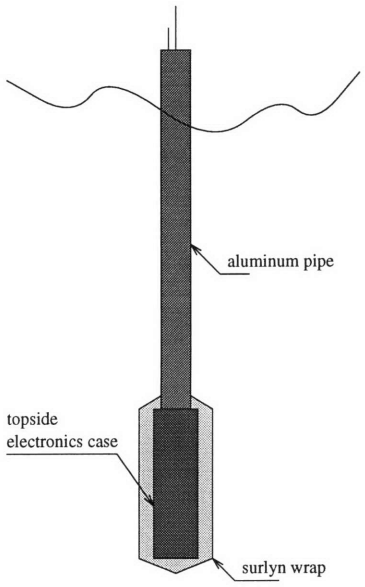

Figure 4-1: Schematic of the proposed spar buoy design.

case to provide buoyancy and fix the total draft of the buoy at 10 m. There is 4 m of freeboard in the design to keep the antennas dry with most passing waves and to provide sufficient reserve buoyancy.

Configuration 7 is the first to use a spar buoy in place of the wave follower currently in use on the SSAR. For comparison purposes, configuration 7 uses the original array cable; it is the same as the baseline SSAR except for the change in the surface buoy. Configurations 8, 9, and 10 use a single flow shielded hydrophone. Configuration 8 uses a six inch outer diameter pipe and configuration 9 uses an eight inch pipe. Though the probability of snap loads is greatly reduced with a spar buoy, both configurations have an extra 200 lbs at the pressure case. Without the additional weight, the hose would be slack in the static configuration. Configuration 10 removes the subsurface float rather than adding weight to keep the hose under tension.

4.3 Discussion

4.3.1 Hydrophone noise

Table 4.5 summarizes all of the noise results for each configuration considered. The noise model for configurations 1 – 4 and 7 is shown in figure 3-6. For configurations 5, 6, and 8 – 10 the appropriate model is figure 3-8. As expected, the configurations using a single flow shielded hydrophone have

	Sea State 4		Sea State 6		
configuration	avg noise	max noise	avg noise	max noise	sea state averaged noise
1	97.96	120.13	102.70	128.09	99.13
2	99.96	122.14	106.04	129.99	101.51
3	99.46	123.34	105.39	131.28	101.07
4	97.37	114.85	103.13	123.76	98.92
5	80.66	88.66	81.94	93.09	81.11
6	80.85	89.89	82.22	94.42	81.34
7	92.51	93.77	95.40	107.89	93.62
8	80.08	80.08	80.08	80.08	80.08
9	80.08	80.08	80.09	81.16	80.10
10	80.08	80.08	80.09	81.13	80.11

Table 4.5: Noise results for each of the modeled SSAR configurations.

significantly lower noise levels than configurations using unshielded hydrophones on an array cable. Within array-based configurations, number 4, which used an extra snubber hose to reduce velocities, was only marginally successful – with only two to three dB improvement in sea state averaged noise and approximately eight dB in maximum instantaneous noise over configurations with comparable hose static tensions (configurations 2 and 3). The results for configuration 7 are another good example of why the SSAR simply will not perform well with an array cable; even with the very low speeds associated with the spar buoy design, the noise is still 10 – 15 dB higher than desirable on average, with peaks that are more than 30 dB greater than the target level.

In comparing designs that use a flow shielded hydrophone, it appears that the flow shield performs sufficiently well at sufficiently high velocities, that the performance of the much slower moving spar-topped configurations (8 – 10) is not significantly better than configurations using the wave follower (5 – 6) in terms of the average noise results. All of the configurations using the flow shield have average noise levels near the ambient given the noise model from the March, 1997 sea trials. The difference in performance is in the maximum noise levels achieved during the ten minute averaging periods. Configurations 5 and 6 (wave following) have maximum noise levels of almost 90 dB in sea state 4 and 94 dB in sea state 6. Configurations 8 – 10, using a spar, have noise maxima that are at the ambient or just slightly above the ambient for the noise model.

Another way to consider the noise levels, particularly in terms of average versus maximum noise levels, is to consider the standard deviations and upcrossing rates of velocity shown in table 4.6 for all configurations. The reason behind the low noise maxima for the spar based models is evident from the small number of times that the velocity exceeds the critical 1.0 m/s level determined by the noise model (figure 3-8). Alternatively, the standard deviation of velocity can be viewed as

	Sea State 4			Sea State 6		
configuration	σ_v (m/s)	n(0.5 m/s)	n(1.0 m/s)	σ_v (m/s)	n(0.5 m/s)	n(1.0 m/s)
1	0.697	90.67	41.89	1.067	84.21	60.57
2	0.725	80.43	39.43	1.113	76.51	56.54
3	0.742	97.16	49.19	1.127	89.49	66.63
4	0.537	59.81	16.27	0.909	63.77	40.49
5	0.787	94.09	51.36	1.187	87.03	66.68
6	0.830	106.65	61.91	1.250	98.33	77.36
7	0.140	0.11	0.00	0.430	26.30	3.46
8	0.043	0.00	0.00	0.248	6.06	0.01
9	0.152	0.29	0.00	0.473	29.65	5.53
10	0.156	0.35	0.00	0.470	29.51	5.41

Table 4.6: Hydrophone velocity results for each of the modeled SSAR configurations. Upcrossing rates are per ten minute averaging cycle.

analogous to the standard deviation of noise. Given this interpretation it is natural that the noise maxima for the spar designs should not be much beyond the noise mean. For the wave following designs the standard deviation of velocity can be as much as five times higher and thus even with low average noise there will be some relatively high noise peaks.

4.3.2 Low ambient modeling

As a final point of consideration, it is informative to apply the noise models with lower ambient noise floors (figures 3-7 and 3-9) to the velocity results of our model configurations. The results of plotting σ_v (from frequency domain results) against time–averaged noise (computed using the low ambient noise models and the time domain model results) for each configuration in each sea state is shown in figure 4-2. The noise model that was applied in this case is shown in figure 3-9. Figure 4-3 does the same thing for acceleration equivalent noise power from figure 3-7.

Given that the lowest resolvable noise levels in both of figures 3-9 and 3-7 are much lower than expected ocean ambient levels, figures 4-2 and 4-3 represent what could be achieved by "optimally" shielded SSAR designs. For instance, if a smaller shield, with flow noise reduction properties similar to the current shield, was developed that could encapsulate the hydrophones on the array cable then the noise level would be dictated by the acceleration-induced noise shown in figure 4-3. In conjunction with a spar buoy, such a design would have noise levels below 80 dB and have the advantage of the full array.

If, on the other hand, the mechanical aspects of the current shield could be improved such that the at-sea noise reduction approached the noise reduction achieved during the Aberdeen experiments,

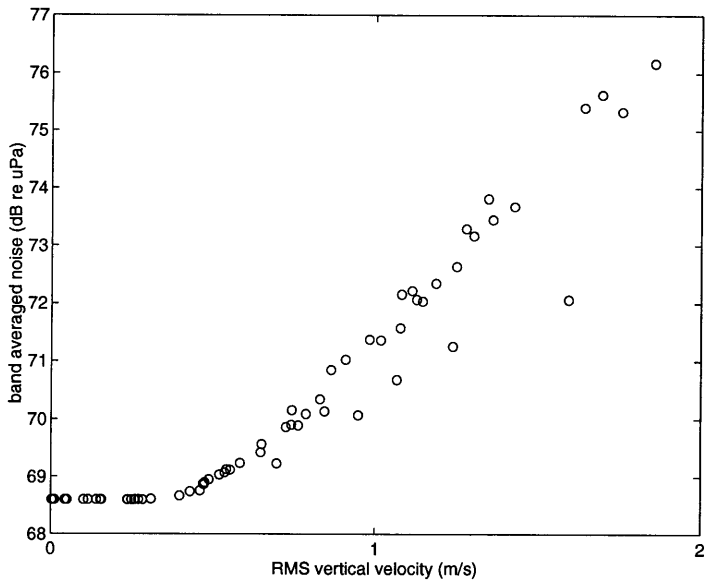

Figure 4-2: Band averaged noise from the low ambient noise model as a function of RMS velocity for each configuration in each sea state.

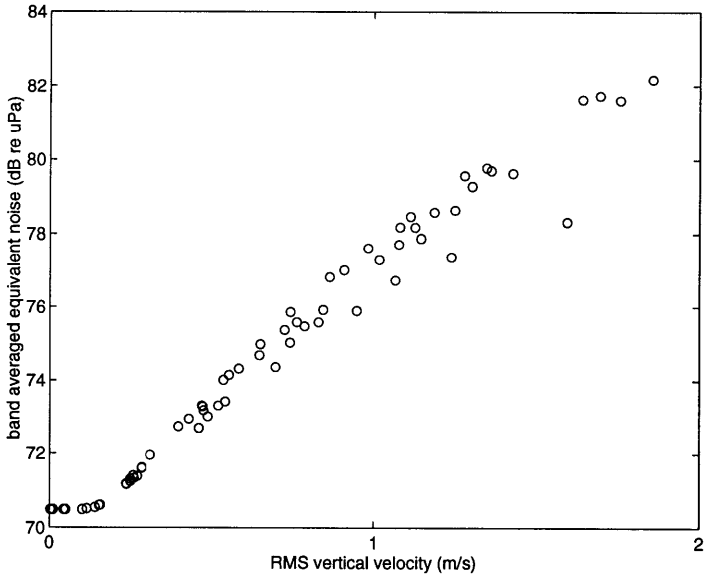

Figure 4-3: Band averaged equivalent noise from the acceleration equivalent noise model as a function of RMS velocity for each configuration in each sea state.

configuration	snap events per year	hose extreme total tension (N)	EM cable extreme total tension (N)	reserve buoyancy (N)
1	4770799	9515	6436	5294
2	294122	12208	9177	3476
3	36441	10224	6892	3404
4	42513	11283	7730	3169
5	1508498	10238	6651	4493
6	27804	9608	5875	3485
7	89507	3194	3448	1305
8	8587	1932	2747	734
9	146928	3149	3169	1305
10	0	3595	2229	1305

Table 4.7: Tension results for each of the modeled SSAR configurations.

the noise would be dictated by a relationship like that shown in figure 4-2. Both spar and wave following buoys can perform acceptably with such a design. With a spar buoy, both the instantaneous and the average flow noise would be lower than ocean ambient in the majority of conditions.

4.3.3 Mechanical performance

Table 4.7 details the important tension statistics for each of the ten model configurations. The results for snap loading are consistent with expectations. It is interesting to note that the statistical prediction for the baseline design (configuration 1) translates to a snap event with almost every passing wave. This is consistent with observations from sea trials (figure 1-3) and is yet another good illustration of the importance of adding static tension in the hose. In comparing configurations 2 and 3, it appears that the better method of achieving this goal is to remove the subsurface float as this does a significantly better job at reducing snap loads for a smaller increase in extreme design tensions.

A second advantage of a spar buoy, in addition to the much lower velocities already discussed, is the much lower tensions that result from the low levels of motion. The configurations using a spar buoy have extreme hose tensions that are as low as one-fifth of the wave following designs. Tensions in the electromechanical cable are generally smaller by at least a factor of two. Configurations 8 and 10 in particular, with their very low snap frequencies (zero for configuration 10) and low extreme tensions, look particularly attractive in terms of system longevity based on both ultimate and fatigue failure criteria.

Table 4.7 also shows the one obvious advantage of the wave following buoy in its larger reserve buoyancy. The six-inch spar buoy which has such good velocity, noise, and tension numbers has

only about half the reserve of the eight-inch spar designs and a fifth of most of the wave following designs.

Chapter 5

Conclusions and Recommendations

5.1 Deployed SSAR systems

The laboratory and at-sea experiments clearly revealed that the SSAR will not perform satisfactorily if the flow-induced noise is not removed. Flow induced noise can easily exceed 100 dB, 10 – 20 dB higher than is acceptable, in relatively low sea-states (vertical velocities of no more than 0.7 m/s). As a consequence, the design chosen for the final six SSARs to be deployed in late 1997 should go as far as possible in trying to eliminate flow noise.

Without an additional research effort to develop an effective, compact, array-mounted flow shield, the advantage offered by the six element array should be sacrificed for the single hydrophone in the large, pressure case mounted flow shield. This approach also removes any acceleration-induced noise associated with hydrophones mounted to an array cable. Additionally, if maximum performance is to be achieved, the wave following surface buoy should be replaced with a spar buoy. A spar buoy will yield additional benefits in terms of system longevity due to reduced motion and tension levels throughout the system.

In order to reduce snap loads in the system, it has already been decided that the subsurface float will be removed and 200 extra pounds added at the subsurface pressure case. The extra 200 pounds essentially replaces the sinker weight that was removed along with the array. This should keep snap loads in the electromechanical cable to a minimum. The subsurface float will be removed, at the cost of a very slight increase in velocities as noted in chapter 4, to provide additional static tension in the hose. This brings the static tension in the hose up to the same level as in the sea trials with extra sinker weight – a level known to be consistent with a large reduction in the number of snap loads.

5.2 Recommendations for future work

The question of the exact source of the acceleration-induced noise is still open. Further research into this area will require a carefully controlled series of experiments with variable sinker masses in a laboratory setting with low mechanical and electrical noise. The interaction between the acceleration-induced noise and the flow noise, and the correlation between the noise signals from adjacent hydrophones that may be resulting from this interaction could also be explored in such a setting.

Though the time domain model proved accurate both in terms of predicting low frequency wave induced motions and the occurrence of snap loads, the way in which a snap load propagates through the system was never fully modeled in this effort. Increasing damping in the electromechanical cable to provide filtering of snap events that occurred in the hose was not practical because the increased damping resulted in erroneously low predictions for the low frequency motions. An additional numerical mechanism is required that will act as a true low-pass filter.

It would also be interesting for future modeling and experimental efforts to explore the accurate modeling of the spectrum of the impulse that results from a snap event. Knowing both the shape and the magnitude of the spectrum as a function of material properties and tension levels is an important consideration in determining the practical implications of snap loading in a system.

Appendix A

Evaluation of Integrals used in the Spar Buoy Modeling

In the frequency domain model the equations for P_1, P_2, $Q_0(k)$, and $Q_1(k)$ (equations 2.33 and 2.34) can be analytically integrated given $S(z)$ defined in a piecewise linear fashion in $N-1$ intervals. Figure A-1 illustrates the notation for the case of the spar used in the model SSAR configurations with four intervals. On the i^{th} interval, from z_i to z_{i+1}, $S(z)$ is written as

$$S(z) = S(z_i) + \beta_i (z - z_i), \tag{A.1}$$

where β_i is defined as

$$\beta_i = \frac{S(z_{i+1}) - S(z_i)}{z_{i+1} - z_i}. \tag{A.2}$$

By substituting this into the integrals of equations 2.33 and 2.34 and breaking the integral into pieces over the intervals of the spar, the integral over each interval can be evaluated directly and the results summed over the intervals.

For P_1 and P_2, the resulting summations are

$$\begin{aligned} P_1 \;=\; & \frac{\rho}{m} \sum_{i=1}^{N-1} \left[z_G \left(\beta_i z_i - S(z_i) \right) \right] (z_{i+1} - z_i) \\ & + \left[S(z_i) - \beta_i (z_i + z_G) \right] \left(\frac{z_{i+1}^2 - z_i^2}{2} \right) + \beta_i \left(\frac{z_{i+1}^3 - z_i^3}{3} \right), \end{aligned} \tag{A.3}$$

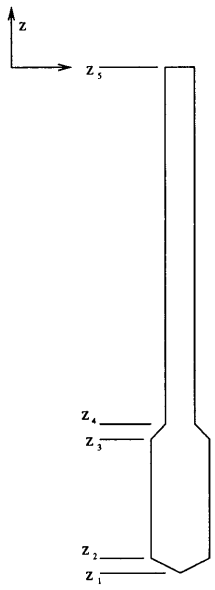

Figure A-1: Piecewise linear geometric description of a spar buoy.

$$
\begin{aligned}
P_2 \;=\; & \frac{\rho}{m}\sum_{i=1}^{N-1}\left[z_G^2\left(S(z_i)-\beta_i z_i\right)\right]\left(z_{i+1}-z_i\right) \\
& +\left[z_G\left(\beta_i z_G-2S(z_i)+2\beta_i z_i\right)\right]\left(\frac{z_{i+1}^2-z_i^2}{2}\right) \\
& +\left[S(z_i)-\beta_i\left(z_i+2z_G\right)\right]\left(\frac{z_{i+1}^3-z_i^3}{3}\right)+\beta_i\left(\frac{z_{i+1}^4-z_i^4}{4}\right).
\end{aligned}
\tag{A.4}
$$

For $Q_0(k)$ and $Q_1(k)$, the final formulas are

$$
Q_0(k)=\frac{\rho}{m}\sum_{i=1}^{N-1}\left[\left(\frac{S(z_i)-\beta_i z_i}{k}\right)-\frac{\beta_i}{k^2}\right]\left(e^{kz_{i+1}}-e^{kz_i}\right)+\frac{\beta_i}{k^2}\left(z_{i+1}e^{kz_{i+1}}-z_i e^{kz_i}\right), \tag{A.5}
$$

$$
\begin{aligned}
Q_1(k) \;=\; & \frac{\rho}{m}\sum_{i=1}^{N-1}\left[\frac{z_G}{k}\left(\beta_i z_i-S(z_i)\right)-\frac{S(z_i)-\beta_i\left(z_i+z_G\right)}{k^2}+\frac{2\beta_i}{k^3}\right]\left(e^{kz_{i+1}}-e^{kz_i}\right) \\
& +\left[\frac{S(z_i)-\beta_i\left(z_i+z_G\right)}{k}-\frac{2\beta_i}{k^2}\right]\left(z_{i+1}e^{kz_{i+1}}-z_i e^{kz_i}\right) \\
& +\frac{\beta_i}{k}\left(z_{i+1}^2e^{kz_{i+1}}-z_i^2e^{kz_i}\right).
\end{aligned}
\tag{A.6}
$$

For the time domain model, the integral used in the evaluation of the Froude–Krylov forces

(equation 2.45) is the same as that for $Q_0(k)$,

$$\begin{aligned}\left(F_w^j\right)_i &= \rho\omega_i^2 A_i \sin\left(j\omega_i\Delta t + t_0 + \phi_i\right)\left\{S(0) - S(-H)e^{-k_i H}\right. \\ &\quad \left. - \sum_{n=1}^{N-1}\left[\left(\frac{S(z_n) - \beta_n z_n}{k_i}\right) - \frac{\beta_n}{k_i^2}\right]\left(e^{k_i z_{n+1}} - e^{k_i z_n}\right) + \frac{\beta_i}{k_i^2}\left(z_{n+1}e^{k_i z_{n+1}} - z_i e^{k_i z_n}\right)\right\}.\end{aligned} \tag{A.7}$$

References

[1] V.H. Arakeri, S.G. Satyanarayana, K. Mani, and S.D. Sharma. Studies on scaling of flow noise received at the stagnation point of an axisymmetric body. *Journal of Sound and Vibration*, 146:449–462, 1991.

[2] Henri O. Berteaux. *Coastal and Oceanic Buoy Engineering.* H.O. Berteaux, Woods Hole, MA, 1991.

[3] Odd M. Faltinsen. *Sea Loads on Ships and Offshore Structures.* Cambridge University Press, Cambridge, 1990.

[4] Andrew Forbes. Acoustic monitoring of global ocean climate. *Sea Technology*, 35:65–67, 1994.

[5] Lee Freitag. Personal communication, March 1997.

[6] Lee Freitag, Daniel Frye, and John Spiesberger. Surface Suspended Acoustic Receiver: A free-drifting acoustic tomography receiver features real-time data processing, telemetry. *Sea Technology*, 36:43–48, 1995.

[7] Daniel E. Frye, Lee Freitag, Walter Paul, Mark Grosenbuagh, and John Spiesberger. Surface Suspended Acoustic Receiver (SSAR) for mapping ocean temperatures. In *Proceedings of Oceanology International 94*, Brighton, UK, 1994.

[8] Mark Grosenbaugh and Spyros Mavrakos. Design of oceanographic surface moorings for harsh weather environments. *SNAME Transactions*, 25, 1995.

[9] G.P. Haddle and E.J. Skudrzyk. The physics of flow noise. *Journal of the Acoustial Society of America*, 46:130–157, 1969.

[10] B.M. Howe, R.W. Gill, C.W. May, and J.H. Morison. Drifters for tomography. In *Proceedings IEEE Oceans 92*, pages 736–741, Newport, RI, 1992.

[11] David W. Hyde. ATOC network definition. In *Proceedings IEEE Oceans 93*, pages 249–252, Victoria, British Columbia, 1993.

[12] Gerald C. Lauchle. Noise generated by axisymmetric turbulent boundary-layer flow. *Journal of the Acoustial Society of America*, 61:694–703, 1977.

[13] Gerald C. Lauchle. Flow noise scaling at the stagnation point of an axisymmetric body. *Journal of Sound and Vibration*, 154:568–572, 1992.

[14] R. Legendre. High velocity acoustics. *Journal of Sound and Vibration*, 157:193–203, 1992.

[15] J.N. Newman. The motions of a spar buoy in regular waves. Technical Report 1499, David Taylor Model Basin, May 1963.

[16] J.N. Newman. *Marine Hydrodynamics.* MIT Press, Cambridge, MA, 1977.

[17] J.L. Spiesberger, D.E. Frye, J. O'Brien, H. Hurlburt, J.W. McCaffrey, M. Johnson, and J. Kenny. Global acoustic mapping of ocean temperature (GAMOT). In *Proceedings IEEE Oceans 93*, pages 253–257, Victoria, British Columbia, 1993.

[18] G.M. Wenz. Acoustic ambient noise in the ocean: spectra and sources. *Journal of the Acoustial Society of America*, 34:1936–1956, 1962.